

# Long-range distribution of multiphoton entanglement

Monika E. Mycroft,<sup>1</sup> Adam Buraczewski,<sup>1</sup> Stefanie Barz,<sup>2,3</sup> and Magdalena Stobińska<sup>1,\*</sup>

<sup>1</sup>*Faculty of Physics, University of Warsaw, ul. Pasteura 5, 02-093 Warsaw, Poland*

<sup>2</sup>*Institute for Functional Matter and Quantum Technologies,  
University of Stuttgart, 70569 Stuttgart, Germany*

<sup>3</sup>*Center for Integrated Quantum Science and Technology,  
University of Stuttgart, IQST, 70569 Stuttgart, Germany*

(Dated: May 8, 2019)

We show that long-distance quantum communications can be enabled through resources provided by current quantum photonic technology: multiphoton bipartite entanglement and photon-number-resolved detection. Our protocol is robust to high transmission losses and facilitates distribution of near-maximally entangled states in realistic implementations. It can be realized in a delayed-choice scheme and it allows one to perform loophole-free Bell tests. The schema discussed can be employed as a versatile source of entanglement for e.g. establishing an Earth-to-space quantum channel, quantum metrology and quantum key distribution.

*Introduction.*— Distribution of photonic entanglement is a key element to building quantum networks which facilitate secure long-distance quantum communications [1], distributed quantum computation [2] and sensing [3]. However, entanglement becomes corrupted by losses in the transmitting channels which results in low transmission rates. Since amplification of quantum signals is impossible [4], alternative remedies are on high demand. One option is to use quantum repeaters [5–11]. However, linking distant parties necessitates numerous intermediate stations, quantum memories and multiple two-photon Bell pairs, a resource that is often created nondeterministically. The other possibility is to use satellites and space-Earth quantum communications as shown recently [12]. In this scheme, Bell-pair entanglement was distributed over 1200 km, which was confirmed by a violation of Bell inequality yet under the fair sampling assumption. Thus, since the aforementioned solutions are challenging in implementation, it remains an open problem how to distribute entanglement in a way that is resource-efficient, verifiable and well suited to the existing quantum-photonic technology.

Here we propose a protocol which allows one to establish long-distance quantum communications based on multiphoton bipartite entanglement and photon-number-resolved detection. It is robust to high symmetric transmission losses which, remarkably, deteriorate only the protocol efficiency, not the amount of generated entanglement. Furthermore, the procedure enables the parties sharing entanglement to perform a loophole-free Bell test.

Bipartite entanglement between two physical systems, such as, for example, two photons is revealed by the fact that outcomes of subsequent local measurements in a certain degree of freedom on these two subsystems are random but always correlated, even when the particles are separated by a large distance [13]. Here, we focus on multi-photon bipartite entanglement. Experimentally,

this type of state can be created by means of spontaneous parametric down-conversion (SPDC) [14]. SPDC sources deterministically produce a two-mode squeezed vacuum (SV). This Gaussian quantum state carries entanglement between quadratures of electric field (continuous variables, CVs) but also between photon numbers in the two modes (discrete variables, DVs), which are unbounded [15]. The latest advances in integrated quantum optics facilitate precise generation and manipulation of SV states in optical chips [16], as well as detection of their photon number statistics using transition-edge sensors (TESs) [17] with quantum efficiency reaching 95% [18].

In our protocol a DV entanglement of high local dimension is created from two sources of an SV state using a generalized Bell measurement. The latter is realized by multiphoton quantum interference on a beam splitter followed by TESs. The protocol can also be realized in a delayed-choice scheme which frees the parties from using quantum memories and allows them to share near-maximally entangled states in realistic implementations. Our setup can also provide entanglement for applications in quantum metrology and quantum key distribution (QKD).

*Resources.*— We employ two copies of an SV state  $|\Psi\rangle$  as our input,  $|\Psi_{\text{in}}\rangle = |\Psi\rangle^{\otimes 2}$ . In its Schmidt basis,  $|\Psi\rangle$  takes the form of a superposition of  $n$ -photon pairs with real-valued probability amplitudes  $\sqrt{\lambda_n} = \frac{\tanh^n g}{\cosh g}$

$$|\Psi\rangle = \sum_{n=0}^{\infty} \sqrt{\lambda_n} |n\rangle_1 |n\rangle_2, \quad (1)$$

where  $g$  is the parametric gain which sets the mean photon number in  $|\Psi\rangle$  to  $2 \sinh^2 g$ . Typically  $g$  is in the range of 0.01–0.1 and one may often assume  $\sqrt{\lambda_n} \approx g^n$ . Perfect quantum correlations in  $|\Psi\rangle$  are manifested by equal photon numbers in modes 1 and 2, called the signal and idler, which can be spatially resolved.

Eq. (1) also shows that the subsequent photon number contributions to the SV state: the vacuum, single-photon and higher-order ( $n > 1$ ) emissions, occur with a prob-

---

\* magdalena.stobinska@gmail.com; Corresponding author

ability which follows a geometric progression of a ratio  $\frac{\lambda_{n+1}}{\lambda_n} = \tanh^2 g$ . Thus, the SPDC generates a considerable amount of multiphoton events also in the regime of weak gain. Our protocol takes advantage of this fact.

*Protocol.*— A scheme of the proposed entanglement distribution is shown in Fig. 1. The setup consists of two SPDC sources, each generating  $|\Psi\rangle$ . The idler beams emitted into modes  $a_2$  and  $b_2$  interfere on a balanced (50 : 50) beam splitter (BS) located on a remote station and then they are detected by TESs. This is an entangling measurement, a multiphoton generalization of the two-photon Bell measurement. As a result of it, the beams  $a_1$  and  $b_1$  become photon-number correlated and an infinite-dimensional input Hilbert space  $\mathcal{H}_{\text{Alice}}^{(\infty)} \otimes \mathcal{H}_{\text{Bob}}^{(\infty)}$  becomes restricted to one of its subspaces of dimension  $d$ ,  $\mathcal{H}_{\text{out}}^{(d)}$ .

Let us consider the lossless case first. The detection of  $S$  photons in total in the Bell measurement means that  $S$  photons distributed between two idler beams entered the BS and also that there are  $S$  photons in the output state. The BS performs a linear operation on the input idler annihilation operators,  $U_{\text{BS}}^\dagger a_2^\dagger U_{\text{BS}} = \frac{1}{\sqrt{2}}(a_2^\dagger - ib_2^\dagger)$ ,  $U_{\text{BS}}^\dagger b_2^\dagger U_{\text{BS}} = \frac{1}{\sqrt{2}}(-ia_2^\dagger + b_2^\dagger)$ , while the signal modes  $a_1$  and  $b_1$  are intact. Applying this operation to Fock states

$$|n\rangle_{a_2} = \frac{(a_2^\dagger)^n}{\sqrt{n!}} |0\rangle, \quad |S-n\rangle_{b_2} = \frac{(b_2^\dagger)^{S-n}}{\sqrt{(S-n)!}} |0\rangle \quad (2)$$

requires taking powers of the transformed operators. This results in a transformation on  $a_2^\dagger$  and  $b_2^\dagger$  governed by a binomial distribution and the output state described by an arcsine probability distribution, see the Supplemental Material (SM) [19]. Through such a multiphoton Hong–Ou–Mandel effect, entanglement between the BS output modes is generated [20]. The probability amplitudes of detecting  $k$  and  $S-k$  photons behind the BS are equal to [21]

$$\begin{aligned} \mathcal{A}_S(k, n) &= \langle k, S-k | U_{\text{BS}} | n, S-n \rangle \\ &= e^{i\frac{\pi}{2}(n-k)} (-1)^{k+n} \phi_k(n - \frac{S}{2}, S). \end{aligned} \quad (3)$$

$\phi_k$ , where  $k = 0, \dots, S$ , are symmetric Kravchuk functions – orthonormal discrete polynomials which converge to Hermite–Gauss polynomials for large  $S$  [22]. The output state in our protocol is therefore

$$\begin{aligned} |\Psi_{\text{out}}^{(k,S)}\rangle &= \mathcal{N} \langle k, S-k | U_{\text{BS}} | \Psi \rangle^{\otimes 2} \\ &= \mathcal{N} \sum_{n,m=0}^{\infty} \sqrt{\lambda_n \lambda_m} |n, m\rangle_{a_1, b_1} \times \\ &\quad \times \langle k, S-k | U_{\text{BS}} | n, m \rangle_{a_2, b_2}, \end{aligned} \quad (4)$$

where  $\mathcal{N}$  is the normalization and  $|\Psi\rangle$  is defined in Eq. 1. Since  $n + m = S$  must hold true,

$$|\Psi_{\text{out}}^{(k,S)}\rangle = \sum_{n=0}^S \mathcal{A}_S(k, n) |n, S-n\rangle_{a_1, b_1}. \quad (5)$$

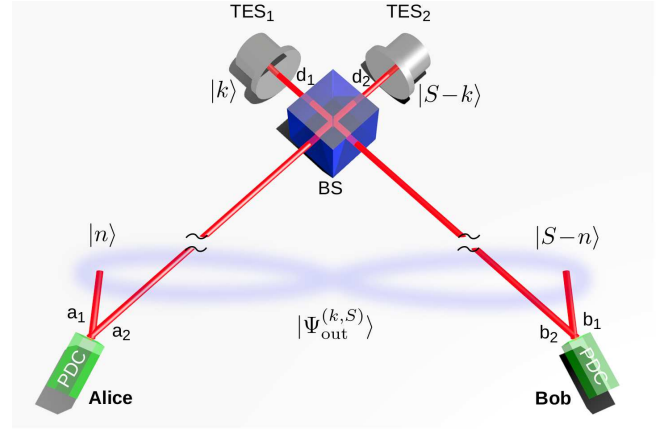


FIG. 1. (Color online) Distribution of multiphoton bipartite entanglement. Alice and Bob locally generate a photon-number entangled two-mode squeezed vacuum state  $|\Psi\rangle$  each. They send their idler modes  $a_2$  and  $b_2$  to a remote station which offers a Bell measurement service. As a result of this entangling measurement, Alice and Bob share a long-range multiphoton DV entanglement in signal modes  $a_1$  and  $b_1$ . The protocol requires the use of two SPDC sources and photon-number-resolving detection.

For details of this derivation see the SM [19].

Thus,  $|\Psi_{\text{out}}^{(k,S)}\rangle$  belongs to a family of states living in an  $(S+1)$ -dimensional Hilbert space  $\mathcal{H}_{\text{out}}^{(S+1)}$  which is created by the conversion of CV entanglement to the DV domain. It is parameterized by the Bell measurement readouts  $k$  and  $S-k$  which define its photon number statistics by setting the probability of detecting  $n$  photons to  $p^{(k,S)}(n) = |\mathcal{A}_S(k, n)|^2 = |\phi_k(n - \frac{S}{2}, S)|^2$ . See the SM for details [19].

This protocol can also be realized in a delayed-choice scheme. Then, the measurement taken by Alice and Bob on the signal modes  $a_1$  and  $b_1$  precedes the one performed on the idler modes  $a_2$  and  $b_2$  at the remote station. Due to entanglement in SV states, the photon-number statistics at Alice’s and Bob’s is again given by  $|\mathcal{A}_S(k, n)|^2$ .

To quantify entanglement in  $|\Psi_{\text{out}}^{(k,S)}\rangle$  we employ the logarithmic negativity  $E_{\mathcal{N}} = \log_2 \|\rho^{\Gamma}\|_1$ , where  $\rho$  denotes a density operator,  $\Gamma$  is the partial transpose operation and  $\|\cdot\|_1$  is the trace norm

$$E_{\mathcal{N}}(|\Psi_{\text{out}}^{(k,S)}\rangle \langle \Psi_{\text{out}}^{(k,S)}|) = 2 \log_2 \left\{ \sum_{n=0}^S \left| \phi_k(n - \frac{S}{2}, S) \right| \right\}. \quad (6)$$

Since the readouts  $k$  and  $S-k$  uniquely define the state  $|\Psi_{\text{out}}^{(k,S)}\rangle$ , they also determine the amount of entanglement in it. In the case of maximally entangled states in a Hilbert space of dimension  $S+1$ ,  $E_{\mathcal{N}_{\text{max}}} = \log_2(S+1)$ . This is the maximal amount of entanglement which can be created in  $\mathcal{H}_{\text{out}}^{(S+1)}$ . Our protocol allows one to achieve values close to the maximal one, as shown in Fig. 2. For a two-photon Bell pair,  $E_{\mathcal{N}_{\text{Bell}}} = 1$ .

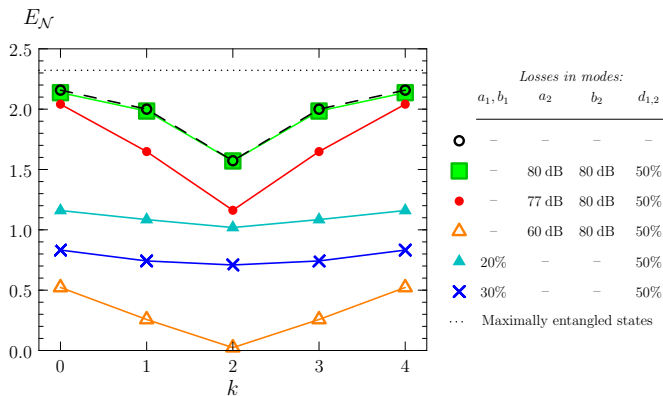


FIG. 2. (Color online) Logarithmic negativity  $E_{\mathcal{N}}$  of  $|\Psi_{\text{out}}^{(k,S)}\rangle$  as a function of detector readouts  $k$  and  $S - k$  in the Bell measurement for  $S = 4$ . Dashed line (empty circles) depicts the ideal case (Eq. 6), while solid lines show numerically computed values for a lossy system: green (filled squares) – large symmetric losses (80 dB attenuation) in the idler modes  $a_2$  and  $b_2$ , red (filled circles) – moderately unsymmetric losses in the idler modes (77–80 dB attenuation), cyan (filled triangles) and blue (crosses) – moderate losses (20% and 30% respectively) in the signal modes  $a_1$  and  $b_1$ , and orange (empty triangles) – hugely unsymmetric losses in the idler modes (60–80 dB attenuation). All nonideal cases were computed for 50% detection efficiency at TESs. The dotted line corresponds to the value of  $E_{\mathcal{N}}$  for maximally entangled states in  $\mathcal{H}_{\text{out}}^{(5)}$ .

Interestingly,  $E_{\mathcal{N}}(|\Psi_{\text{out}}^{(k,S)}\rangle \langle \Psi_{\text{out}}^{(k,S)}|)$  does not depend on the parametric gain  $g$ . This might be counterintuitive since one would expect that entanglement conversion would perform better for higher amounts of the initial entanglement used. For the SV  $E_{\mathcal{N}}(|\Psi\rangle \langle \Psi|) = 2g/\ln 2$ , and in the limit of infinite squeezing,  $g \rightarrow \infty$ , it tends to the maximally entangled Einstein–Podolsky–Rosen state [23, 24]. Our protocol allows one to obtain high amount of entanglement even for weakly squeezed SVs, at a cost of the overall efficiency which equals  $\lambda_S$ , see the SM [19]. For a pulsed SPDC source, the efficiency can be improved by increasing the intensity and repetition rate  $f_{\text{rep}}$  of the pump. For example, for  $g = 0.1$  and  $f_{\text{rep}} = 80$  MHz, the protocol produces ca.  $45$  4-photon and  $4.6 \times 10^5$  2-photon entangled pairs per minute, see the SM [19] for details of the calculation.

*Real-world applications.*– Long-distance photon transmission is affected by attenuation, ranging from 0.2 dB/km for telecommunication fibers to ca. 80 dB for a space-to-Earth channel of 2400 km [12]. The efficiency of a detection system including TESs may drop to 50–60% due to losses and inefficient coupling.

Losses are modeled by inserting additional BSs into the pathways of the photons. Their reflectivity  $r$  quantifies the amount of loss. Numerical calculations were performed for different scenarios: the ideal case, the case of large symmetric losses in the idler beams ( $r_{a_2, b_2} = 99.999999\%$ , i.e. 80 dB), the case of large unsymmet-

ric losses in the idler beams with small (50% or 3 dB) and largest reasonable (20 dB) difference between them ( $r_{a_2} = 99.999998\%$ ,  $r_{b_2} = 99.999999\%$ , i.e. 77, 80 dB and  $r_{a_2} = 99.99999\%$ ,  $r_{b_2} = 99.9999999\%$  i.e. 60, 80 dB respectively). We also show the case of nonideal signal modes with 20% and 30% loss in those arms. In all nonideal cases we set realistic losses at the detectors ( $r_{d_1, d_2} = 50\%$ ), however, their influence is negligible. The most relevant results are presented in Fig. 2. For further details see the SM [19].

Our numerical computations show that the protocol is robust to an arbitrarily high attenuation in the idler modes, as long as it is symmetric. This fact is also revealed by an analytical decomposition of the output state density operator into the following sum  $\tilde{\rho}_{\text{out}}^{(k,\sigma)} = \sum_{S=\sigma}^{\infty} \chi_{\sigma,S} \tilde{\rho}_{\text{int}}^{(\sigma,k,S)}$ , where  $\tilde{\rho}_{\text{int}}^{(\sigma,k,S)}$  is a density operator of a state with  $S$  photons in total in the signal modes which are lossless, created by  $\sigma - k$  and  $k$  readouts at the Bell measurement station, with probability  $\chi_{\sigma,S} = r^{\sigma-S} \lambda_S \binom{S+1}{\sigma+1}$ , see the SM [19]. In  $\tilde{\rho}_{\text{out}}^{(k,\sigma)}$ , the amount of entanglement we obtain “per shot” is probabilistic. However, the most likely event is  $\tilde{\rho}_{\text{int}}^{(S,k,S)}$  which is identical to  $|\Psi_{\text{out}}^{(k,S)}\rangle \langle \Psi_{\text{out}}^{(k,S)}|$ . Since  $\chi_{\sigma,S}$  drops rapidly towards zero for  $S > \sigma$ , this renders the remaining components practically irrelevant. Closer inspection of  $\tilde{\rho}_{\text{out}}^{(k,\sigma)}$  reveals that losses scale down the parametric gain  $g$  and thus, they influence only the efficiency of the protocol, which is now equal to  $(1-r)^\sigma \lambda_\sigma$ , without changing its principle of operation. This feature is characteristic to protocols based on two-photon Bell pair entanglement and now we have shown it also for a multiphoton setup. It is worth mentioning that robustness of our protocol to symmetric losses is crucial from the engineering point of view. It corresponds to the common design of transmission channels in telecommunications. Such balanced lines allow one to easily reject external noise and common-mode interference. Nevertheless, our numerical computations indicate that the system performs well also for unsymmetrical losses with the logarithmic negativity remaining within 90% of the original values even when the relative transmittance of the channels drops to 0.4, see the SM [19]. One also needs to consider that the loss for each channel will vary with time [25]. However, losses fluctuate on timescales an order of magnitude higher than the time of flight of photons, therefore it suffices to take the average of Alice and Bob’s output logarithmic negativity. The effect of fluctuations on the average is not detrimental, see the SM [19].

Detection inefficiencies or losses in signal modes  $a_1$  and  $b_1$  are critical since they spoil generated entanglement, see the SM [19].

*Application to Earth-space communications.*– It is interesting to compare our protocol with the remarkable satellite-based entanglement distribution demonstrated in [12]. There, an SPDC source pumped by a CW laser generated spaceborne Bell pairs at random times, which were next sent by a downlink channel to two mutually re-

mote stations on Earth. The entanglement between the stations was verified by a Clauser–Horne–Shimony–Holt Bell test. However, this scheme was based on postselection and thus, on the fair sampling hypothesis. Due to losses, only one Bell pair from ca.  $10^6$  reached the stations per second. The rate of the source was estimated by a classical weak measurement (0.01% of the beam). A classical two-way communication between Alice and Bob was necessary to discard the cases when only one of the stations received a photon. The single-photon detectors used could not discriminate between single- and multiphoton inputs.

In contrast, in our protocol Alice and Bob each create locally an SV state. Their sources can be synchronized offline by e.g. precise clocks. A Bell measurement station, e.g. located on a satellite, performs a conditional state preparation. It acts as a central authority which broadcasts via a classical downlink if Alice and Bob share an entangled state. Thus, neither communication between the parties nor filtering out the vacuum or the higher-order emissions is required. In an actual Earth-space quantum communications implementation, a success rate of Alice and Bob sharing an entangled state is expected to reach 1.6 Hz [19] compared to 0.54 Hz found in [12]. Moreover, the protocol in a form of a delayed-choice experiment frees the parties from the use of quantum memories and allows them to minimize losses in the signal modes.

An important feature of this scheme is that it allows Alice and Bob to perform a Bell test on the whole ensemble of the prepared states without sampling them. This, combined with the use of photodetectors of high efficiency closes the detection loophole and paves the way to performing a genuine loophole-free Bell test [26–28].

In addition, the measurement outcomes at the Bell station allow Alice and Bob to choose the dimensionality of their local Hilbert spaces and thus, control the amount of shared entanglement. A family of noise-resistant Bell inequalities for bipartite quantum systems of arbitrarily high local dimension is already known [29]. Alternatively, other methods can be employed if a polarization degree of freedom comes into play. This can be achieved by extending the local resources to four-mode polarization-entangled SV [30, 31]. It is done by using two SPDC crystals and producing two copies of two-mode SV state per party [24].

*Conclusions.*– We have proposed a long-range entanglement distribution protocol based on an optimal use of the existing quantum integrated optical components. The protocol is feasible: an experiment which constitutes its proof of concept has been reported in [21]. Unique features that make it an interesting alternative to the existing solutions comprise robustness to arbitrarily high transmission losses, ability of choosing local dimension of the generated entangled state and the possibility of performing a loophole-free Bell test by adopting a preselection instead of postselection procedure. Its efficiency is comparable to the state-of-the-art solutions and can be further tuned. Thus, we believe that our protocol can compete with e.g. recently deployed space-to-Earth entanglement generation setup [12].

Until now, robustness of entanglement to losses has been an exclusive feature of solutions based on single-photon technology. Here we demonstrate it also for setups which employ multiphoton entanglement that is naturally generated by commonly available sources of quantum light. This is important since creation of two-photon entanglement requires additional effort.

Our scheme can be useful beyond the context of entanglement distribution.  $|\Psi_{\text{out}}^{(k,S)}\rangle$  is a generalized Holland–Burnett (HB) state, which becomes a HB state for  $k = S/2$  [32]. It offers quantum-enhanced optical phase estimation [33]. For almost all  $k$ ,  $|\Psi_{\text{out}}^{(k,S)}\rangle$  can be employed in quantum metrological tasks. The values of quantum Fisher information computed for  $|\Psi_{\text{out}}^{(k,S)}\rangle$  are shown in the SM [19]. In addition, since two-mode Fock states are mutually orthogonal, they can serve as a mean for multi-letter QKD.

## ACKNOWLEDGMENTS

*Acknowledgments.*– We would like to thank Christine Silberhorn and Tim Bartley for discussions. MM, AB and MS were supported by the Foundation for Polish Science “First Team” project POIR.04.04.00-00-220E/16-00 (FIRST TEAM/2016-2/17). Numerical computations were performed in the ACK “Cyfronet” AGH computer center (Zeus cluster). SB acknowledges support from the CarlZeiss Foundation and from the Federal Ministry of Education and Research (BMBF, project SiSiQ).

- 
- [1] N. Gisin and R. Thew, *Quantum communication*, Nat. Photonics **1**, 165 (2007).
  - [2] J. I. Cirac, A. K. Ekert, S. F. Huelga, and C. Macchiavello, *Distributed quantum computation over noisy channels*, Phys. Rev. A **59**, 4249 (1999).
  - [3] Z. Eldredge, M. Foss-Feig, J. A. Gross, S. Rolston, and A. V. Gorshkov, *Optimal and secure measurement protocols for quantum sensor networks*, Phys. Rev. A **97**, 042337 (2018).
  - [4] W. K. Wootters and W. H. Zurek, *A single quantum cannot be cloned*, Nature **299**, 802 (1982).
  - [5] N. Sangouard, C. Simon, H. De Riedmatten, and N. Gisin, *Quantum repeaters based on atomic ensembles and linear optics*, Rev. Mod. Phys. **83**, 33 (2011).
  - [6] W. J. Munro, A. M. Stephens, S. J. Devitt, K. A. Harrison, and K. Nemoto, *Quantum communication without the necessity of quantum memories*, Nat. Photonics **6**, 777 (2012).

- [7] S. Muralidharan, J. Kim, N. Lütkenhaus, M. D. Lukin, and L. Jiang, *Ultrafast and Fault-Tolerant Quantum Communication across Long Distances*, Phys. Rev. Lett. **112**, 250501 (2014).
- [8] K. Azuma, K. Tamaki and H.-K. Lo, *All-photonic quantum repeaters*, Nat. Commun. **6**, 6787 (2015).
- [9] P. van Loock, T. D. Ladd, K. Sanaka, F. Yamaguchi, K. Nemoto, W. J. Munro, and Y. Yamamoto, *Hybrid Quantum Repeater Using Bright Coherent Light*, Phys. Rev. Lett. **96**, 240501 (2006).
- [10] J. B. Brask, I. Rigas, E. S. Polzik, U. L. Andersen, and A. S. Sørensen, *Hybrid Long-Distance Entanglement Distribution Protocol*, Phys. Rev. Lett. **108**, 219901 (2012).
- [11] M. Zwerger, A. Pirker, V. Dunjko, H. J. Briegel, and W. Dür, *Long-Range Big Quantum-Data Transmission*, Phys. Rev. Lett. **120**, 030503 (2018).
- [12] J. Yin, Y. Cao, Y.-H. Li, S.-K. Liao, L. Zhang, J.-G. Ren, W.-Q. Cai, W.-Y. Liu, B. Li, H. Dai *et al.*, *Satellite-based entanglement distribution over 1200 kilometers*, Science **356**, 1140 (2017).
- [13] R. Horodecki, P. Horodecki, M. Horodecki, and K. Horodecki, *Quantum entanglement*, Rev. Mod. Phys. **81**, 865 (2009).
- [14] J. W. Pan, Z.-B. Chen, C.-Y. Lu, H. Weinfurter, A. Zeilinger, and M. Żukowski, *Multiphoton entanglement and interferometry*, Rev. Mod. Phys. **84**, 777 (2012).
- [15] M. V. Chekhova, G. Leuchs, and M. Żukowski, *Bright squeezed vacuum: Entanglement of macroscopic light beams*, Opt. Commun. **337**, 27 (2015).
- [16] F. Lenzini, J. Janousek, O. Thearle, M. Villa, B. Haylock, S. Kasture, L. Cui, H.-P. Phan, D. V. Dao, H. Yonezawa *et al.*, *Integrated photonic platform for quantum information with continuous variables*, Sci. Adv. **4**, eaat9331 (2018).
- [17] T. Gerrits, N. Thomas-Peter, J. C. Gates, A. E. Lita, B. J. Metcalf, B. Calkins, N. A. Tomlin, A. E. Fox, A. L. Linares, J. B. Spring *et al.*, *On-chip, photon-number-resolving, telecommunication-band detectors for scalable photonic information processing*, Phys. Rev. A **84**, 060301 (2011).
- [18] A. E. Lita, A. J. Miller, and S. W. Nam, *Counting near-infrared single-photons with 95% efficiency*, Opt. Express **16**, 3032 (2008).
- [19] See Supplemental Material at [URL will be inserted by publisher] for additional derivations and results of numerical computations.
- [20] M. S. Kim, W. Son, V. Bužek, and P. L. Knight, *Entanglement by a beam splitter: Nonclassicality as a prerequisite for entanglement*, Phys. Rev. A **65**, 032323 (2002).
- [21] M. Stobińska, A. Buraczewski, M. Moore, W. R. Clements, J. J. Renema, S. W. Nam, T. Gerrits, A. Lita, W. S. Kolthammer, A. Eckstein, and I. A. Walmsley, *Quantum interference enables constant-time quantum information processing*, arXiv:1807.03960 (2018).
- [22] N. M. Atakishiyev and K. B. Wolf, *Fractional Fourier-Kravchuk transform*, J. Opt. Soc. Am. A **14**, 1467 (1997).
- [23] B.-G. Englert and K. Wódkiewicz, *Separability of two-party Gaussian states*, Phys. Rev. A **65**, 054303 (2002).
- [24] M. Stobińska, F. Töppel, P. Sekatski, and M. V. Chekhova, *Entanglement witnesses and measures for bright squeezed vacuum*, Phys. Rev. A **86**, 022323 (2012).
- [25] J.-P. Bourgoin, E. Meyer-Scott, B. L. Higgins, B. Helou, C. Erven, H. Hübel, B. Kumar, D. Hudson, I. D'Souza, R. Girard *et al.*, *A comprehensive design and performance analysis of low Earth orbit satellite quantum communication*, New J. Phys. **15**, 023006 (2013).
- [26] M. Stobińska, P. Sekatski, A. Buraczewski, N. Gisin, and G. Leuchs, *Bell-inequality tests with macroscopic entangled states of light*, Phys. Rev. A **84**, 034104 (2011).
- [27] M. Giustina, A. Mech, S. Ramelow, B. Wittmann, J. Kofler, J. Beyer, A. Lita, B. Calkins, T. Gerrits, S. W. Nam *et al.*, *Bell violation using entangled photons without the fair-sampling assumption*, Nature **497**, 227 (2013).
- [28] A. Peres, *Bell inequalities with postselection*, Boston Stud. Philos. Sci. **194**, 191 (Kluwer, 1997).
- [29] D. Collins, N. Gisin, N. Linden, S. Massar, and S. Popescu, *Bell Inequalities for Arbitrarily High-Dimensional Systems*, Phys. Rev. Lett. **88**, 040404 (2002).
- [30] K. Rosolek, M. Stobińska, M. Wieśniak, and M. Żukowski, *Two copies of the Einstein-Podolsky-Rosen State of Light Lead to Refutation of EPR Ideas*, Phys. Rev. Lett. **114**, 100402 (2015).
- [31] A. Rutkowski, A. Buraczewski, P. Horodecki, and M. Stobińska, *Quantum Steering Inequality with Tolerance for Measurement-Setting Errors: Experimentally Feasible Signature of Unbounded Violation*, Phys. Rev. Lett. **118**, 020402 (2017).
- [32] M. J. Holland and K. Burnett, *Interferometric detection of optical phase shifts at the Heisenberg limit*, Phys. Rev. Lett. **71**, 1355 (1993).
- [33] A. Datta, L. Zhang, N. Thomas-Peter, U. Dörner, B. J. Smith, and I. A. Walmsley, *Quantum metrology with imperfect states and detectors*, Phys. Rev. A **83**, 063836 (2011).
- [34] T. Hakioglu and K. B. Wolf, *The canonical Kravchuk basis for discrete quantum mechanics*, J. Phys. A: Math. and Gen. **33**, 3313 (2000).
- [35] H. Nakazato, S. Pascazio, M. Stobińska, and K. Yuasa, *Photon distribution at the output of a beam splitter for imbalanced input states*, Phys. Rev. A **93** 023845 (2016).
- [36] R. Demkowicz-Dobrzański, M. Jarzyna, and J. Kołodyński, *Quantum limits in optical interferometry*, in *Progress in Optics*, Vol. **60**, p. 345 (Elsevier, 2015).

## Supplemental Material: Long-range distribution of multiphoton entanglement

This Supplemental Material is composed of six sections. The first is devoted to the characterization of  $|\Psi_{\text{out}}^{(k,S)}\rangle$ . By means of analytical calculations, we derive formulas quantifying its logarithmic negativity and quantum Fisher information. In Section II we present an analytical proof that the protocol is robust to symmetric losses occurring before the Bell measurement (i.e. in modes  $a_2$  and  $b_2$ , as shown in Fig. 1 in the main text) and include numerical computations validating our derivations. The proof also verifies that these losses reduce the protocol's efficiency while keeping the amount of generated entanglement constant (between modes  $a_1$  and  $b_1$ ). In Section III we perform a similar analysis of the unsymmetric losses case. We show that these losses have the effect of reducing the dimension of the Hilbert space in which the family of the output states lives. Our derivations are confirmed by numerical simulations. In Section IV we consider the effect of time variation of transmittance and find that it lowers the time-averaged logarithmic negativity. Section V is devoted to success rates. We give an estimation of the expected success rate in a realistic setting. The computer program we have developed and used is described in Section VI.

### I. ANALYTICAL EXPRESSIONS CHARACTERIZING THE PROTOCOL IN THE LOSSLESS CASE

#### A. Photon number statistics for the output state $|\Psi_{\text{out}}^{(k,S)}\rangle$

The family of output states generated by our protocol is given in Eq. (3) in the main text

$$|\Psi_{\text{out}}^{(k,S)}\rangle = \sum_{n=0}^S \mathcal{A}_S(k, n) |n, S-n\rangle_{a_1, b_1}, \quad (\text{S1})$$

where  $S$  is the total number of photons distributed between the idler modes and the probability amplitudes  $\mathcal{A}_S(k, n)$  are expressed using symmetric Kravchuk functions  $\phi_k$  [21]

$$\mathcal{A}_S(k, n) = \langle k, S-k | U_{\text{BS}} |n, S-n\rangle = e^{i\frac{\pi}{2}(n-k)} (-1)^{k+n} \phi_k(n - S/2, S). \quad (\text{S2})$$

In probability theory, Kravchuk polynomials  $k_k(n, S)$  describe a binomial process of a random walk on a line [22]. They form solutions of the Kravchuk difference equation which is a discrete counterpart of the Hermite differential equation [34].  $k_k(n, S)$  satisfy discrete orthogonality and completeness relations. Kravchuk functions are defined in terms of Kravchuk polynomials, normalized and multiplied by the root of the binomial distribution

$$\phi_k(n - S/2, S) = \sqrt{\frac{k!(S-k)!}{n!(S-n)!}} \left(\frac{1}{2}\right)^{S-2k} k_k(n, S). \quad (\text{S3})$$

They create an orthonormal set with respect to the binomial distribution for  $k = 0, \dots, S$ . Figs. S1–S2 and S3–S4 depict exemplary Kravchuk functions  $\phi_k(n - S/2, S)$  and photon number distributions  $|\mathcal{A}_S(k, n)|^2 = |\phi_k(n - S/2, S)|^2$  for  $S = 4$  and 10 and  $k = 0, \dots, S$ , respectively.

Additionally, for  $k = S/2$ , the probability distribution  $|\mathcal{A}_S(S/2, n)|^2$  possesses an envelope  $f(n) = \frac{4}{\pi S \sqrt{1 - (2n/S - 1)^2}}$  which is a probability density function of an arcsine distribution [35].

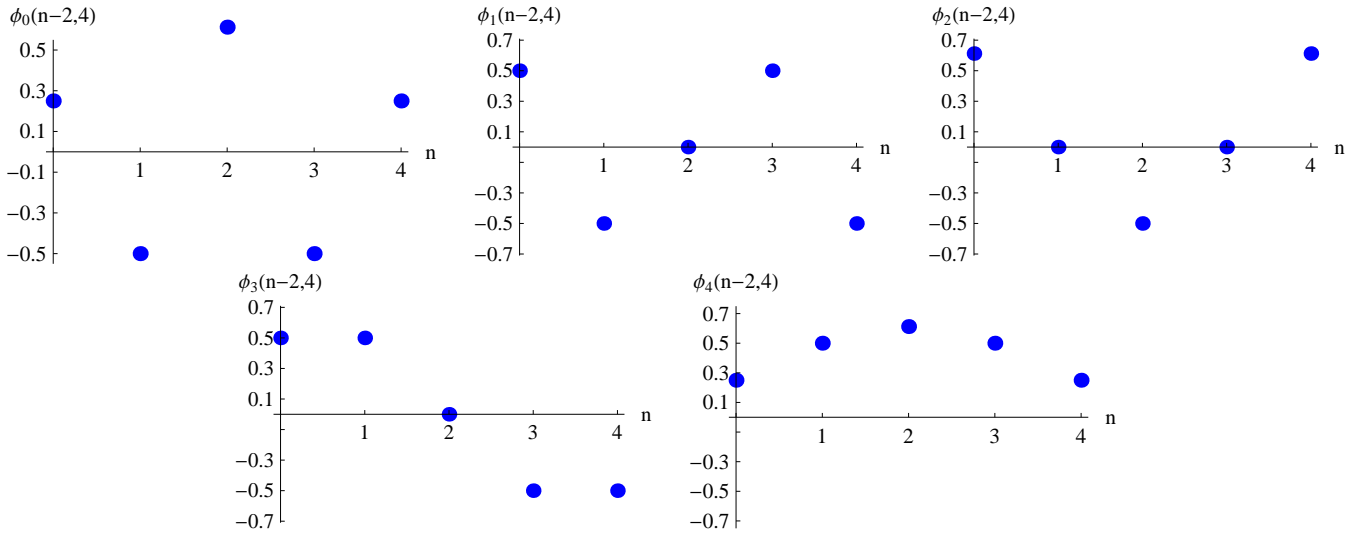


FIG. S1. Symmetric Kravchuk functions  $\phi_k(n - S/2, S)$  computed for  $S = 4$  and  $k = 0, \dots, 4$ .

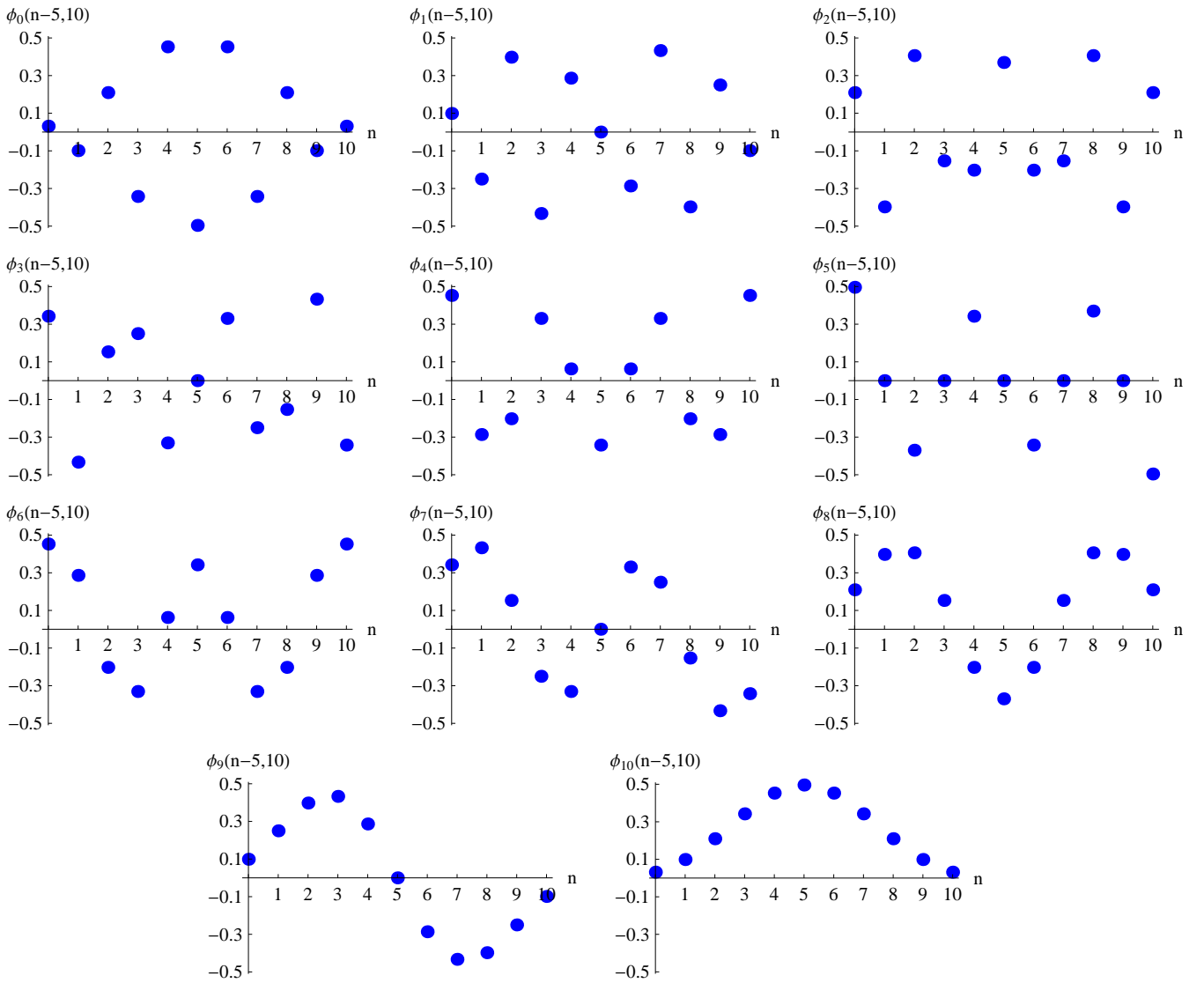


FIG. S2. Symmetric Kravchuk functions  $\phi_k(n - S/2, S)$  computed for  $S = 10$  and  $k = 0, \dots, 10$ .

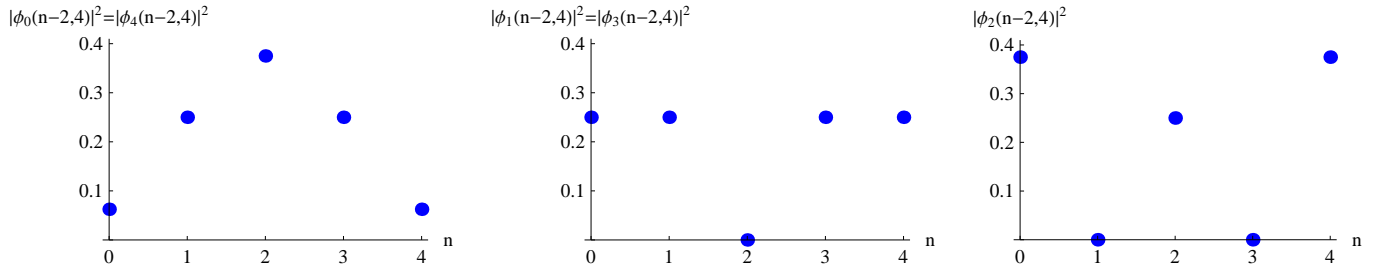


FIG. S3. Photon number distributions  $|\mathcal{A}_S(k, n)|^2 = |\phi_k(n - S/2, S)|^2$  computed for  $S = 4$  and  $k = 0, 1, 2$ .

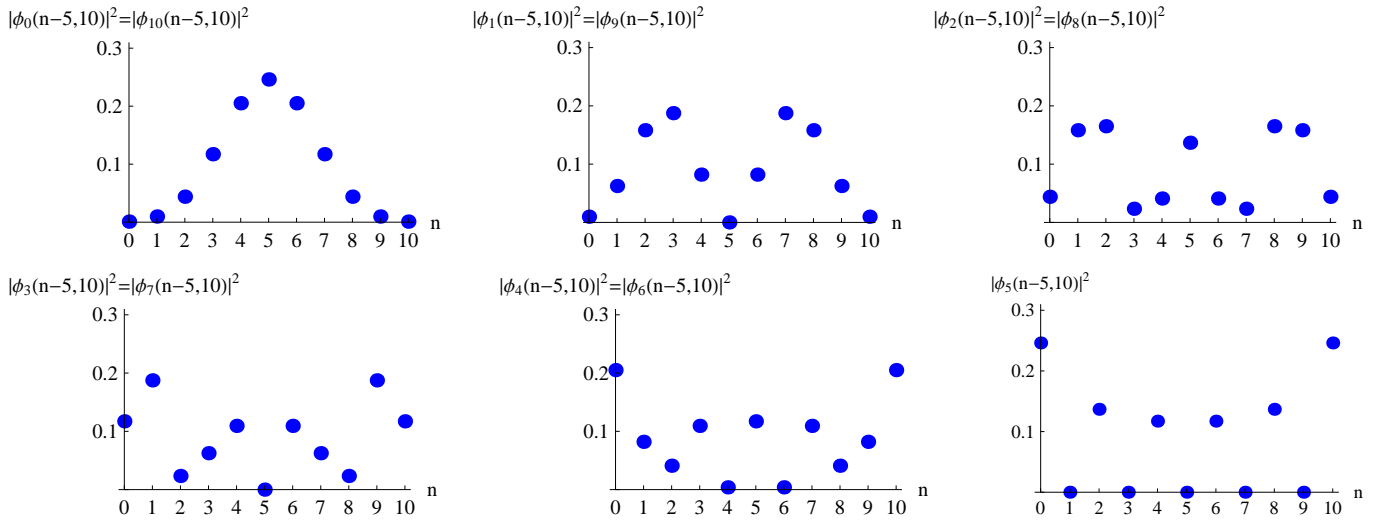


FIG. S4. Photon number distributions  $|\mathcal{A}_S(k, n)|^2 = |\phi_k(n - S/2, S)|^2$  computed for  $S = 10$  and  $k = 0, \dots, 5$ .

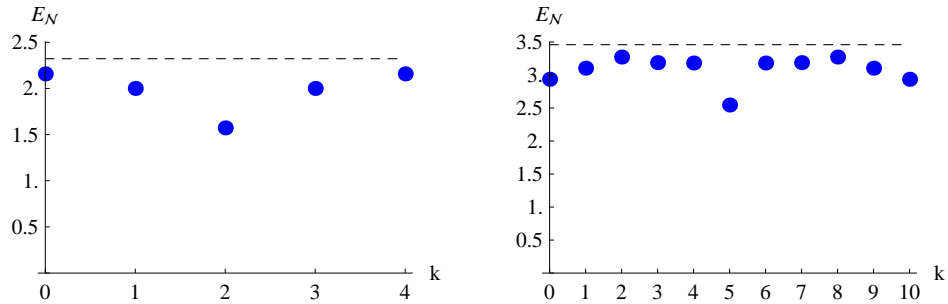


FIG. S5. Logarithmic negativity  $E_{\mathcal{N}}(\rho_{\text{out}}^{(k,S)})$  given in Eq. (S4) computed for  $S = 4$  (left) and  $S = 10$  (right). The dashed lines denote the value of logarithmic negativity obtained for a maximally entangled state,  $E_{\mathcal{N}_{\text{max}}} = \log_2(S + 1)$ .



### B. Logarithmic negativity for $|\Psi_{\text{out}}^{(k,S)}\rangle$

Logarithmic negativity of a physical state given by a density operator  $\rho$  is defined as  $E_{\mathcal{N}}(\rho) = \log_2 \|\rho^\Gamma\|_1$ , where  $\Gamma$  denotes the partial transposition operation and  $\|\rho^\Gamma\|_1$  is the trace norm of  $\rho^\Gamma$ . For  $|\Psi_{\text{out}}^{(k,S)}\rangle$  it equals

$$E_{\mathcal{N}}(\rho_{\text{out}}^{(k,S)}) = 2 \log_2 \left( \sum_n^S |\mathcal{A}_S(k, n)| \right). \quad (\text{S4})$$

This formula can be derived in the following way

$$\rho_{\text{out}}^{(k,S)} = |\Psi_{\text{out}}^{(k,S)}\rangle \langle \Psi_{\text{out}}^{(k,S)}| = \sum_{n,m=0}^S \underbrace{[\rho]_{n,S-n;m,S-m}}_{\mathcal{A}_S(k,n)\mathcal{A}_S^*(k,m)} |n, S-n\rangle \langle m, S-m|, \quad (\text{S5})$$

$$\left(\rho_{\text{out}}^{(k,S)}\right)^{\Gamma_2} = \sum_{n,m=0}^S [\rho]_{n,S-n;m,S-m} |n, S-m\rangle \langle m, S-n|, \quad (\text{S6})$$

$$\left(\left(\rho_{\text{out}}^{(k,S)}\right)^{\Gamma_2}\right)^\dagger = \sum_{n,m=0}^S [\rho]_{n,S-n;m,S-m}^* |m, S-n\rangle \langle n, S-m|, \quad (\text{S7})$$

$$\left(\left(\rho_{\text{out}}^{(k,S)}\right)^{\Gamma_2}\right)^\dagger \cdot \left(\rho_{\text{out}}^{(k,S)}\right)^{\Gamma_2} = \sum_{n,m,p,q=0}^S [\rho]_{n,S-n;m,S-m}^* [\rho]_{p,S-p;q,S-q} |m, S-n\rangle \langle n, S-m| p, S-q\rangle \langle q, S-p| \quad (\text{S8})$$

$$= \sum_{n,m,p,q=0}^S [\rho]_{n,S-n;m,S-m}^* [\rho]_{p,S-p;q,S-q} \delta_{n,p} \delta_{m,q} |m, S-n\rangle \langle q, S-p| \quad (\text{S9})$$

$$= \sum_{n,m=0}^S [\rho]_{n,S-n;m,S-m}^* [\rho]_{n,S-n;m,S-m} |m, S-n\rangle \langle m, S-n| \quad (\text{S10})$$

$$= \sum_{n,m=0}^S |[\rho]_{n,S-n;m,S-m}|^2 |m\rangle \langle m| \otimes |S-n\rangle \langle S-n|, \quad (\text{S11})$$

$$\left(\left(\rho_{\text{out}}^{(k,S)}\right)^{\Gamma_2}\right)^\dagger \cdot \left(\rho_{\text{out}}^{(k,S)}\right)^{\Gamma_2} = \sum_{n,m=0}^S |\mathcal{A}_S(k, n)|^2 |\mathcal{A}_S(k, m)|^2 |m\rangle \langle m| \otimes |S-n\rangle \langle S-n| \quad (\text{S12})$$

$$= \left( \sum_n^S |\mathcal{A}_S(k, n)|^2 |S-n\rangle \langle S-n| \right) \otimes \left( \sum_{m=0}^S |\mathcal{A}_S(k, m)|^2 |m\rangle \langle m| \right). \quad (\text{S13})$$

The above operator is diagonal and therefore, it is easy to compute the square root of it by taking the square root of its eigenvalues

$$\sqrt{\left(\left(\rho_{\text{out}}^{(k,S)}\right)^{\Gamma_2}\right)^\dagger \cdot \left(\rho_{\text{out}}^{(k,S)}\right)^{\Gamma_2}} = \left( \sum_n^S |\mathcal{A}_S(k, n)| |S-n\rangle \langle S-n| \right) \otimes \left( \sum_{m=0}^S |\mathcal{A}_S(k, m)| |m\rangle \langle m| \right), \quad (\text{S14})$$

$$\left\| \left(\rho_{\text{out}}^{(k,S)}\right)^{\Gamma_2} \right\|_1 = \text{Tr} \sqrt{\left(\left(\rho_{\text{out}}^{(k,S)}\right)^{\Gamma_2}\right)^\dagger \cdot \left(\rho_{\text{out}}^{(k,S)}\right)^{\Gamma_2}} = \sum_{a,b=0}^S \left( \sum_n^S |\mathcal{A}_S(k, n)| \langle a|S-n\rangle \langle S-n|a\rangle \right) \left( \sum_{m=0}^S |\mathcal{A}_S(k, m)| \langle b|m\rangle \langle m|b\rangle \right) \quad (\text{S15})$$

$$= \left( \sum_n^S |\mathcal{A}_S(k, n)| \right)^2. \quad (\text{S16})$$

In these formulas,  $\delta_{n,m}$  denotes the Kronecker delta, equal to 1 for  $n = m$  and 0 otherwise.

$E_{\mathcal{N}}(\rho_{\text{out}}^{(k,S)})$  is depicted in Fig. S5. It is compared to the value of logarithmic negativity obtained for a maximally entangled state  $E_{\mathcal{N}_{\text{max}}}$ .

### C. Quantum Fisher Information for $|\Psi_{\text{out}}^{(k,S)}\rangle$

Quantum Fisher Information (QFI) of a quantum state gives the upper bound on precision of a parameter estimation which can be achieved using this state. It allows us to assess usefulness of a quantum state for quantum metrology. For  $|\Psi_{\text{out}}^{(k,S)}\rangle$  the QFI can be computed using the following formula [36]

$$F_Q(\rho_{\text{out}}^{(k,S)}) = 4 \left[ \sum_{n=0}^S |\mathcal{A}_S(k,n)|^2 n^2 - \left( \sum_{n=0}^S |\mathcal{A}_S(k,n)|^2 n \right)^2 \right]. \quad (\text{S17})$$

For comparison, the value of QFI for Holland–Burnett states, which are created if  $k = S/2$ , is equal to  $F_Q(\text{HB}) = 2N(N+1)$ , where  $N = S/2$ .

Exemplary  $F_Q(\rho_{\text{out}}^{(k,S)})$  and  $F_Q(\text{HB})$  are shown in Fig. S6.

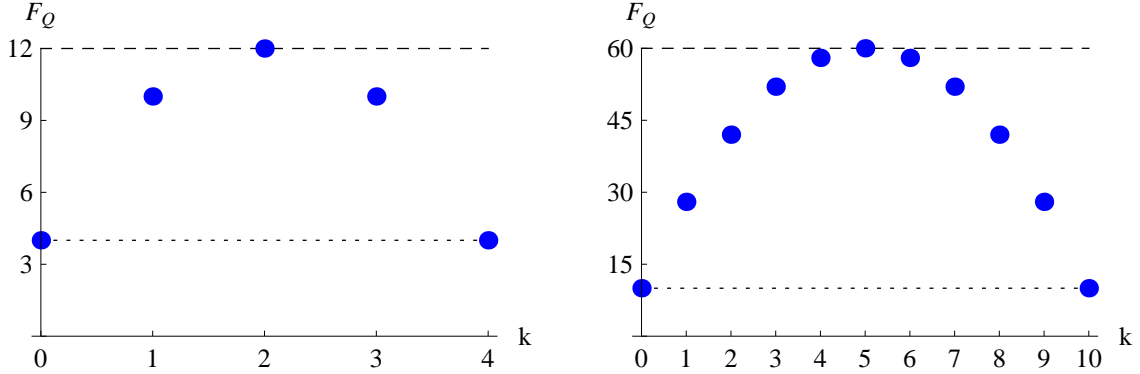


FIG. S6. Quantum Fisher Information  $F_Q(\rho_{\text{out}}^{(k,S)})$  given in Eq. (S17) computed for  $S = 4$  (left) and  $S = 10$  (right). The dashed lines give the values of QFI obtained for Holland–Burnett states,  $F_Q(\text{HB}) = S(S/2 + 1)$ . The dotted lines show the shot-noise limit.

## II. PROTOCOL PERFORMANCE IN CASE OF SYMMETRIC LOSSES IN IDLER MODES $a_2$ AND $b_2$

### A. Ideal case revisited

An SV state is given by

$$|\Psi\rangle = \sum_{n=0}^{\infty} \sqrt{\lambda_n} |n\rangle_1 |n\rangle_2. \quad (\text{S18})$$

Density operator for the input state  $|\Psi_{\text{in}}\rangle = |\Psi\rangle^{\otimes 2}$  is as follows

$$\rho_{\text{in}} = \sum_{n,n',m,m'=0}^{\infty} \sqrt{\lambda_n \lambda_{n'} \lambda_m \lambda_{m'}} |n, m\rangle \langle n', m'|_{a_1, b_1} \otimes |n, m\rangle \langle n', m'|_{a_2, b_2}. \quad (\text{S19})$$

Modes  $a_2$  and  $b_2$  interfere on a beam splitter and the resulting output modes are projected onto  $|k, S-k\rangle_{d_1, d_2}$ . Let  $S$  denote the total number of photons registered behind the BS. In the ideal case, it is equal to the total number of photons in the remaining modes  $a_1$  and  $b_1$ . The state created in modes  $a_1$  and  $b_1$  takes the form

$$\rho_{\text{out}}^{(k,S)} = \mathcal{N}^2 \sum_{n,n',m,m'=0}^{\infty} \delta_{S,n+m} \delta_{S,n'+m'} \sqrt{\lambda_n \lambda_{n'} \lambda_m \lambda_{m'}} \mathcal{A}_S^{(1/2)}(k,n) (\mathcal{A}_S^{(1/2)}(k,n'))^* |n, m\rangle \langle n', m'|_{a_1, b_1}, \quad (\text{S20})$$

where  $\mathcal{N}^2 = \frac{\cosh^4 g}{\tanh^{2S} g}$ . This simplifies to

$$\rho_{\text{out}}^{(k,S)} = \sum_{n,n'=0}^S \mathcal{A}_S^{(1/2)}(k,n) (\mathcal{A}_S^{(1/2)}(k,n'))^* |n, S-n\rangle \langle n', S-n'|_{a_1, b_1}. \quad (\text{S21})$$

## B. Analytic derivations

Here we assume no losses in signal modes  $a_1$  and  $b_1$ , as well as ideal detection performed by all four TES detectors.

Losses can be modelled by a beam splitter with reflectivity  $r \in [0, 1]$  which quantifies the amount of loss. For a Fock state  $|n\rangle$  it reduces to

$$\text{Tr}_r \left\{ U_{\text{BS}}^{(r)} |n, 0\rangle \langle n, 0| \left( U_{\text{BS}}^{(r)} \right)^\dagger \right\} = \sum_{p=0}^n \binom{n}{p} (1-r)^{n-p} r^p |n-p\rangle \langle n-p|_t, \quad (\text{S22})$$

where  $t$  and  $r$  denote the transmitted and reflected mode, respectively,  $r + t = 1$ , and

$$U_{\text{BS}}^{(r)} |n, 0\rangle = \sum_{p=0}^n \sqrt{\binom{n}{p}} (1-r)^{n-p} r^p |n-p, p\rangle_{t,r}. \quad (\text{S23})$$

For  $r = 0$  it reduces to  $\text{Tr}_r \left\{ U_{\text{BS}}^{(0)} |n, 0\rangle \langle n, 0| \left( U_{\text{BS}}^{(0)} \right)^\dagger \right\} = |n\rangle \langle n|_t$ .

Applying this procedure to the input state  $|\Psi_{\text{in}}\rangle$  leads to

$$\begin{aligned} \rho_{\text{in}} = & \sum_{n,n',m,m'=0}^{\infty} \sqrt{\lambda_n \lambda_{n'} \lambda_m \lambda_{m'}} \sum_{p=0}^{\min(n,n')} \sum_{q=0}^{\min(m,m')} \sqrt{\binom{n}{p} \binom{n'}{p} (1-r_a)^{n+n'-2p} r_a^{2p}} \times \\ & \times \sqrt{\binom{m}{q} \binom{m'}{q} (1-r_b)^{m+m'-2q} r_b^{2q}} \times \\ & \times |n, m\rangle \langle n', m'|_{a_1, b_1} \otimes |n-p, m-q\rangle \langle n'-p, m'-q|_{a_2, b_2}, \end{aligned} \quad (\text{S24})$$

where  $r_a$  and  $r_b$  denote losses at Alice's and Bob's idler modes. As we assume that there are no losses in modes  $a_1$  and  $b_1$ , the total number of photons in these modes equals  $S = n + m = n' + m'$ . The lossy modes  $a_2$  and  $b_2$  interfere on a balanced beam splitter and are projected onto  $|k, \sigma - k\rangle_{d_1, d_2}$ , where  $\sigma \leq S$ . In case of no losses,  $\sigma = S$ . This results in the creation of the following state

$$\begin{aligned} \tilde{\rho}_{\text{out}}^{(k,\sigma)} = & \tilde{\mathcal{N}}^2 \sum_{n,n',m,m'=0}^{\infty} \sqrt{\lambda_n \lambda_{n'} \lambda_m \lambda_{m'}} |n, m\rangle \langle n', m'|_{a_1, b_1} \times \\ & \times \sum_{p=0}^{\min(n,n')} \sum_{q=0}^{\min(m,m')} \sqrt{\binom{n}{p} \binom{n'}{p} (1-r_a)^{n+n'-2p} r_a^{2p}} \sqrt{\binom{m}{q} \binom{m'}{q} (1-r_b)^{m+m'-2q} r_b^{2q}} \times \\ & \times \mathcal{A}_\sigma^{(1/2)}(k, n-p) \left( \mathcal{A}_\sigma^{(1/2)}(k, n'-p) \right)^* \delta_{\sigma, n+m-p-q} \delta_{\sigma, n'+m'-p-q}, \end{aligned} \quad (\text{S25})$$

where

$$\frac{1}{\tilde{\mathcal{N}}^2} = \sum_{n,m=0}^{\infty} \lambda_n \lambda_m \sum_{p=\max(0, n-\sigma)}^{\min(n, n+m-\sigma)} \binom{n}{p} \binom{m}{n+m-\sigma-p} (1-r_a)^{n-p} r_a^p (1-r_b)^{p+\sigma-n} r_b^{n+m-p-\sigma} \left| \mathcal{A}_\sigma^{(1/2)}(k, n-p) \right|^2. \quad (\text{S26})$$

We now assume that the losses are equal, i.e.  $r_a = r_b = r$ . Then,

$$(1-r)^{n+n'-2p} r^{2p} (1-r)^{m+m'-2q} r^{2q} = (1-r)^{2\sigma} r^{n+m+n'+m'-2\sigma}. \quad (\text{S27})$$

This allows us to write

$$\begin{aligned} \tilde{\rho}_{\text{out}}^{(k,\sigma)} = & \tilde{\mathcal{N}}^2 \sum_{n,n',m,m'=0}^{\infty} r^{-\sigma} \sqrt{r^n \lambda_n r^{n'} \lambda_{n'} r^m \lambda_m r^{m'} \lambda_{m'}} |n, m\rangle \langle n', m'|_{a_1, b_1} \times \\ & \times \sum_{p=0}^{\min(n,n')} \sum_{q=0}^{\min(m,m')} \sqrt{\binom{n}{p} \binom{n'}{p} \binom{m}{q} \binom{m'}{q}} \times \\ & \times \mathcal{A}_\sigma^{(1/2)}(k, n-p) \left( \mathcal{A}_\sigma^{(1/2)}(k, n'-p) \right)^* \delta_{\sigma, n+m-p-q} \delta_{\sigma, n'+m'-p-q}. \end{aligned} \quad (\text{S28})$$

Since  $S = n + m = n' + m'$ , we notice that  $n, n' \leq S$  and  $\sigma = S - p - q$ . Since  $q = S - \sigma - p$ , we are able to remove the sum over  $q$ , which creates constraints on  $p$ :  $p \leq S - \sigma$  and  $p \geq n - \sigma$  as well as  $p \geq n' - \sigma$ . The state takes the form

$$\begin{aligned} \tilde{\rho}_{\text{out}}^{(k,\sigma)} &= \tilde{\mathcal{N}}^2 \sum_{S=\sigma}^{\infty} \sum_{n,n'=0}^S r^{-\sigma} \sqrt{r^n \lambda_n r^{n'} \lambda_{n'} r^{S-n} \lambda_{S-n} r^{S-n'} \lambda_{S-n'}} |n, S-n\rangle \langle n', S-n'|_{a_1, b_1} \times \\ &\quad \times \sum_{p=0}^{\min(n,n')} \sum_{q=0}^{\min(S-n, S-n')} \sqrt{\binom{n}{p} \binom{n'}{p} \binom{S-n}{q} \binom{S-n'}{q}} \times \\ &\quad \times \mathcal{A}_{\sigma}^{(1/2)}(k, n-p) \left( \mathcal{A}_{\sigma}^{(1/2)}(k, n'-p) \right)^* \delta_{\sigma, S-p-q} \end{aligned} \quad (\text{S29})$$

$$\begin{aligned} &= \tilde{\mathcal{N}}^2 \sum_{S=\sigma}^{\infty} r^{S-\sigma} \lambda_S \sum_{n,n'=0}^S |n, S-n\rangle \langle n', S-n'|_{a_1, b_1} \times \\ &\quad \times \sum_{p=\max(0, n-\sigma, n'-\sigma)}^{\min(S-\sigma, n, n')} \sqrt{\binom{n}{p} \binom{n'}{p} \binom{S-n}{S-\sigma-p} \binom{S-n'}{S-\sigma-p}} \times \\ &\quad \times \mathcal{A}_{\sigma}^{(1/2)}(k, n-p) \left( \mathcal{A}_{\sigma}^{(1/2)}(k, n'-p) \right)^* \end{aligned} \quad (\text{S30})$$

$$= \tilde{\mathcal{N}}^2 \sum_{S=\sigma}^{\infty} \frac{r^{S-\sigma} \lambda_S}{\tilde{\mathcal{N}}_{\text{int}}^2} \tilde{\rho}_{\text{int}}^{(\sigma, k, S)} = \tilde{\mathcal{N}}^2 \sum_{S=\sigma}^{\infty} \chi_{\sigma, S} \tilde{\rho}_{\text{int}}^{(\sigma, k, S)}, \quad (\text{S31})$$

where  $\chi_{\sigma, S} = \frac{r^{S-\sigma} \lambda_S}{\tilde{\mathcal{N}}_{\text{int}}^2}$  and Eq. (S26) simplifies to

$$\frac{1}{\tilde{\mathcal{N}}^2} = \sum_{S=\sigma}^{\infty} r^{S-\sigma} \lambda_S \sum_{n=0}^S \sum_{p=\max(0, n-\sigma)}^{\min(S-\sigma, n)} \binom{n}{p} \binom{S-n}{S-\sigma-p} \left| \mathcal{A}_{\sigma}^{(1/2)}(k, n-p) \right|^2. \quad (\text{S32})$$

The internal matrix is as follows

$$\begin{aligned} \tilde{\rho}_{\text{int}}^{(\sigma, k, S)} &= \tilde{\mathcal{N}}_{\text{int}}^2 \sum_{n,n'=0}^S |n, S-n\rangle \langle n', S-n'|_{a_1, b_1} \times \\ &\quad \times \sum_{p=\max(0, n-\sigma, n'-\sigma)}^{\min(S-\sigma, n, n')} \sqrt{\binom{n}{p} \binom{n'}{p} \binom{S-n}{S-\sigma-p} \binom{S-n'}{S-\sigma-p}} \times \\ &\quad \times \mathcal{A}_{\sigma}^{(1/2)}(k, n-p) \left( \mathcal{A}_{\sigma}^{(1/2)}(k, n'-p) \right)^*, \end{aligned} \quad (\text{S33})$$

where

$$\frac{1}{\tilde{\mathcal{N}}_{\text{int}}^2} = \sum_{n=0}^S \sum_{p=\max(0, n-\sigma)}^{\min(S-\sigma, n)} \binom{n}{p} \binom{S-n}{S-\sigma-p} \left| \mathcal{A}_{\sigma}^{(1/2)}(k, n-p) \right|^2. \quad (\text{S34})$$

We have numerically proven that for  $0 < S \leq 1000$  and  $0 \leq \sigma \leq S$ ,  $\frac{1}{\tilde{\mathcal{N}}_{\text{int}}^2} = \binom{S+1}{\sigma+1}$ . This allows to simplify the form of  $\chi_{\sigma, S}$  to

$$\chi_{\sigma, S} = r^{S-\sigma} \lambda_S \binom{S+1}{\sigma+1}. \quad (\text{S35})$$

From Eq. (S31) we see that  $r^{S-\sigma}$  scales  $\lambda_S$  directly and it does not influence the overall structure of the state. For  $S = \sigma$ , as expected,  $\tilde{\rho}_{\text{int}}^{(\sigma,k,S)}$  reproduces the density operator for the lossless case

$$\begin{aligned} \tilde{\rho}_{\text{int}}^{(S,k,S)} &= \sum_{n,n'=0}^S |n, S-n\rangle \langle n', S-n'|_{a_1, b_1} \times \\ &\quad \times \sum_{p=\max(0, n-S, n'-S)}^{\min(S-S, n, n')} \sqrt{\binom{n}{p} \binom{n'}{p} \binom{S-n}{S-S-p} \binom{S-n'}{S-S-p}} \times \\ &\quad \times \mathcal{A}_S^{(1/2)}(k, n-p) \left( \mathcal{A}_S^{(1/2)}(k, n'-p) \right)^* \end{aligned} \quad (\text{S36})$$

$$= \sum_{n,n'=0}^S \mathcal{A}_S^{(1/2)}(k, n) \left( \mathcal{A}_S^{(1/2)}(k, n') \right)^* |n, S-n\rangle \langle n', S-n'|_{a_1, b_1} = \rho_{\text{out}}^{(k,S)}. \quad (\text{S37})$$

The coefficient  $\chi_{\sigma,S} = r^{S-\sigma} \lambda_S / \tilde{\mathcal{N}}_{\text{int}}^2$  quantifies the contribution of  $\tilde{\rho}_{\text{int}}^{(\sigma,k,S)}$  to the final density operator. It obtains the highest value for  $S = \sigma$ ,  $\chi_{S,S} = \lambda_S$ , and monotonically decreases for  $S > \sigma$ . Fig. S7 depicts its values for  $g = 0.1$ ,  $\sigma = 4$  and  $r = 0.5$ .

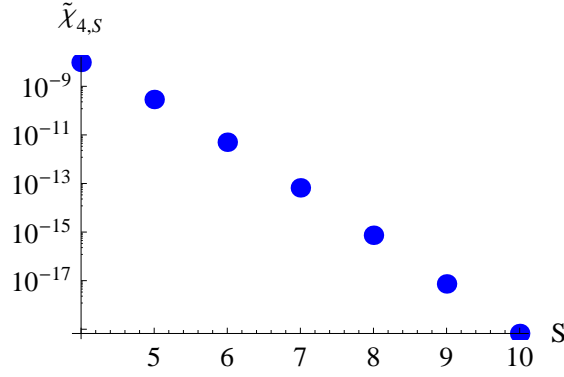


FIG. S7.  $\chi_{\sigma,S}$  computed for  $r = 0.5$ ,  $g = 0.1$  and  $\sigma = 4$ .

### C. Numerical computations

We have computed the logarithmic negativity for the density operator in Eq. S30 assuming losses  $r_i$  in idler modes  $a_2$  and  $b_2$  to be symmetric. All remaining losses (at signal modes and detectors) have been set to zero. As is customary, the reflectivities in the results below and in the following subsections are displayed in percentages (%).

We have changed  $r_i$  between 0 and 90%. The case of  $r_i = 99.999999\%$  (80 dB), which is typical of Earth-to-space scenarios, has been also examined. The results are shown in Fig. S8. The logarithmic negativity is not deteriorated by increasing values of  $r_i$  and even for  $r_i = 99.999999\%$  it is close to the ideal case.

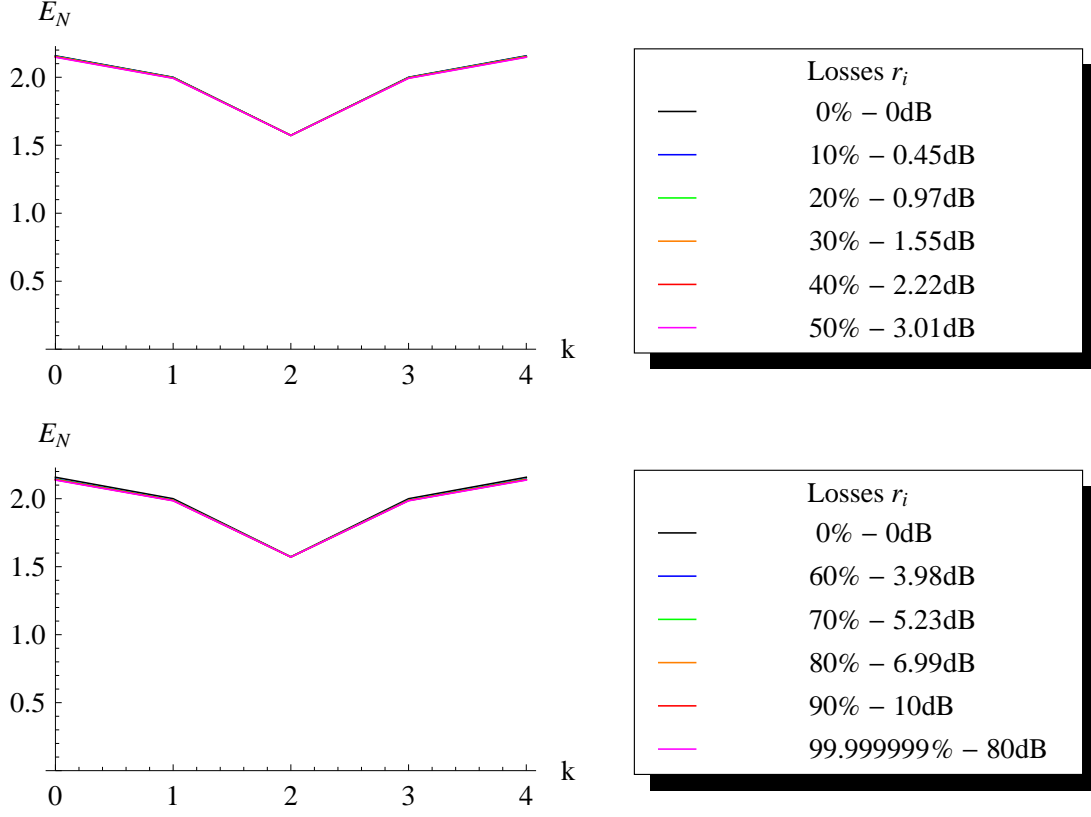


FIG. S8. Logarithmic negativity of the state given in Eq. S30 computed for  $g = 0.1$  and  $S = 4$  assuming symmetric losses in idler modes  $a_2$  and  $b_2$  with losses in remaining modes and at the detectors set to zero.

### D. Numerical computations including lossy detection

We have repeated the above computations for the density operator in Eq. S30 with nonzero losses  $r_d$  at the TESs located behind the beam splitter included in the numerical programme. Fig. S9 depicts the values of  $E_N$  for  $r_d$  equal to 5% and 28%, which correspond to detector efficiency of 95% and 72%, respectively. We have also set the range of  $r_i \in [0, 99.999999\%]$ . Similarly to the previous case, the results are not deteriorated by the losses.

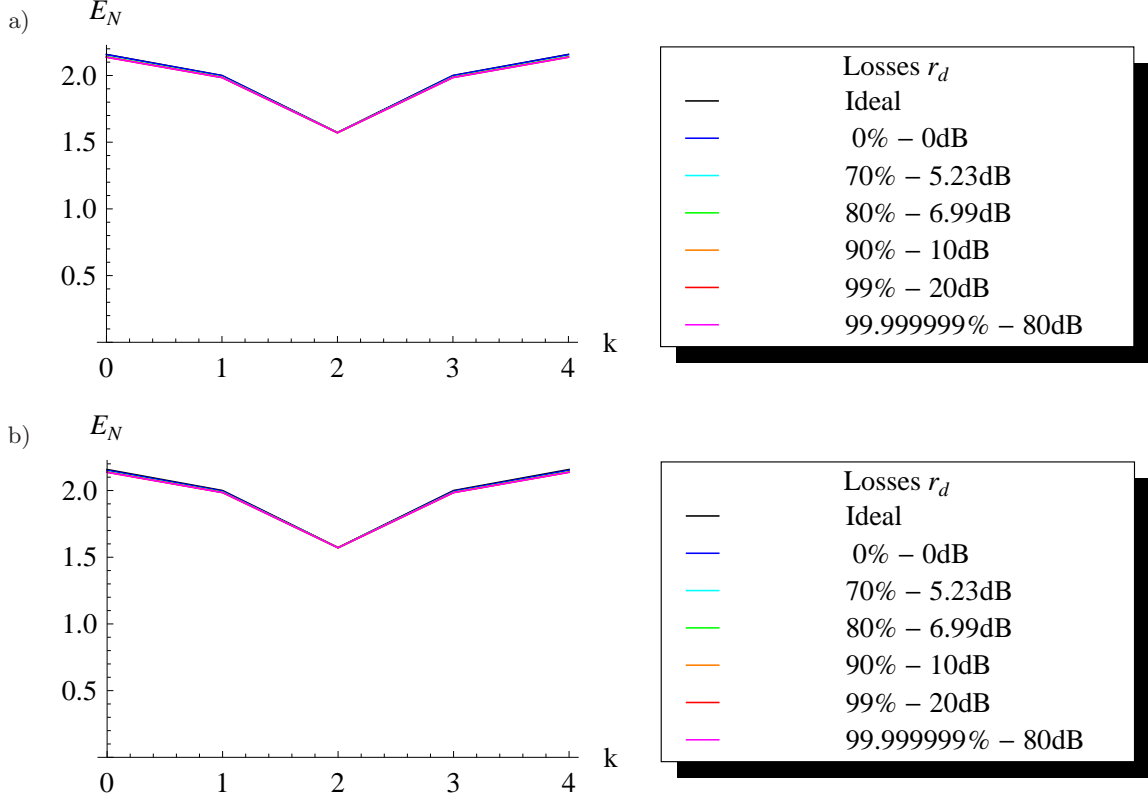


FIG. S9. Logarithmic negativity of the state given in Eq. S30 computed for  $g = 0.1$  and  $S = 4$  assuming symmetric losses in idler modes  $a_2$  and  $b_2$  and losses at the detectors located behind the beam splitter set to a) 5% b) 28%. The losses at signal modes are set to zero.

### E. Comparison with the case of symmetric losses in signal modes $a_1$ and $b_1$

In order to check the influence of losses  $r_s$  in signal modes  $a_1$  and  $b_1$  we have set them to symmetric values in the range between 0 and 50%. The losses at the detectors have been set to 5% and 28% while we assumed no losses at idler modes. The results are depicted in Fig. S10. Nonzero values of  $r_s$  significantly lower the obtained logarithmic negativity, which drops below 1.0 for  $g = 0.1$ ,  $S = 4$  and  $r_s = 30\%$ .

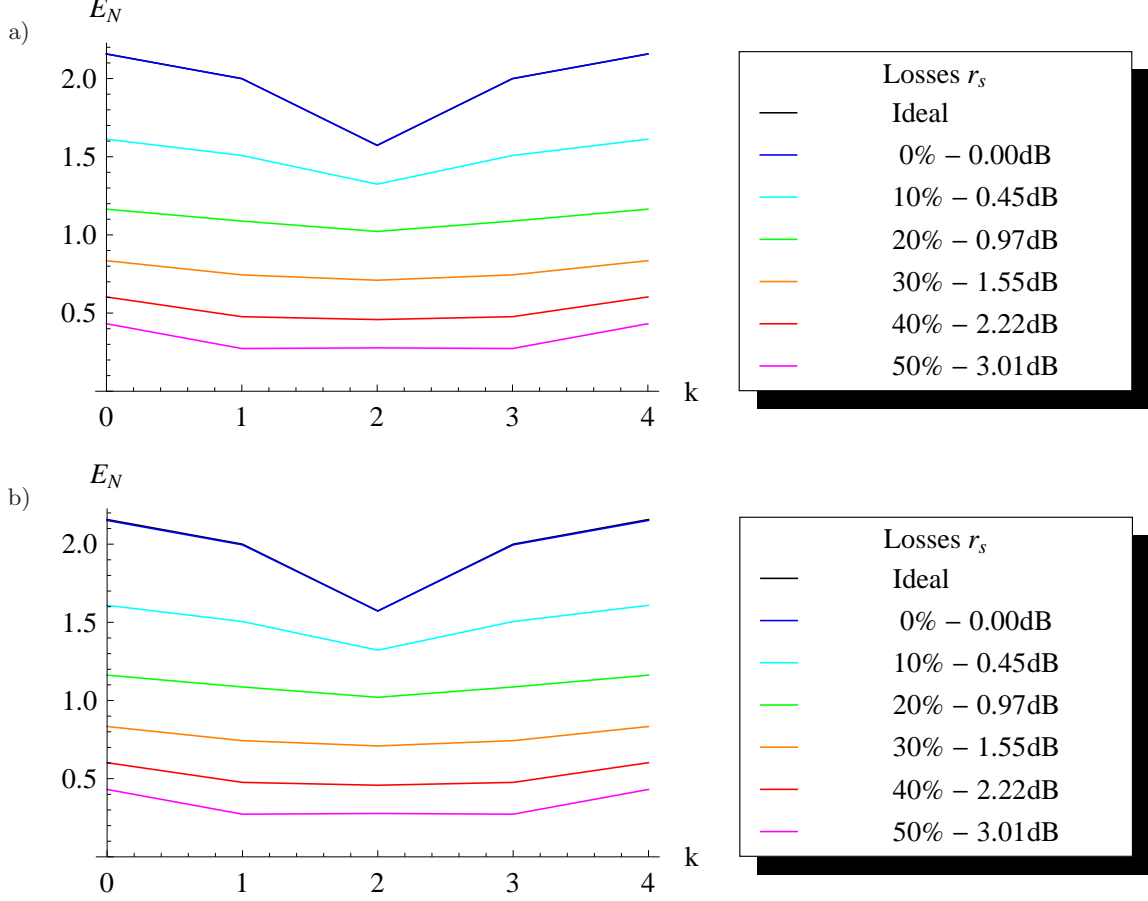


FIG. S10. Logarithmic negativity computed for  $g = 0.1$  and  $S = 4$  assuming symmetric losses in signal modes  $a_1$  and  $b_1$  and losses at the detectors located behind the beam splitter set to a) 5% b) 28%. The losses at idler modes are set to zero.



### III. PROTOCOL PERFORMANCE FOR UNSYMMETRIC LOSSES IN IDLER MODES $a_2$ AND $b_2$

#### A. Analytic derivations

In this subsection we assume no losses in signal modes as well as ideal detection performed by all four TES detectors. Moreover, since analytical derivations become quite complex for a general case of losses occurring in our setup, we will first analyze the case when Bob's idler mode,  $b_2$ , is lossless ( $t_b = 1$  or  $r_b = 0$ ) and Alice's idler mode's transmittance,  $t_a$ , is a fraction  $\epsilon$  of Bob's mode's transmittance ( $t_a = \epsilon$ ). This approach will allow us to understand the impact of unsymmetric losses on the protocol's performance.

We repeat the steps as in Subsection IIB but with  $r_a = 1 - \epsilon$  to arrive at the form equivalent to Eq. (S25)

$$\begin{aligned} \tilde{\rho}_{\text{out}}^{(k,\sigma)} &= \tilde{\mathcal{N}}^2 \sum_{n,n',m,m'=0}^{\infty} \sqrt{\lambda_n \lambda_{n'} \lambda_m \lambda_{m'}} |n, m\rangle \langle n', m'|_{a_1, b_1} \times \\ &\times \sum_{p=0}^{\min(n,n')} \sum_{q=0}^{\min(m,m')} \sqrt{\binom{n}{p} \binom{n'}{p} t_a^{n+n'-2p} (1-t_a)^{2p}} \sqrt{\binom{m}{q} \binom{m'}{q} t_b^{m+m'-2q} (1-t_b)^{2q}} \times \\ &\times \mathcal{A}_{\sigma}^{(1/2)}(k, n-p) \left( \mathcal{A}_{\sigma}^{(1/2)}(k, n'-p) \right)^* \delta_{\sigma, n+m-p-q} \delta_{\sigma, n'+m'-p-q} \end{aligned} \quad (\text{S38})$$

$$\begin{aligned} &= \tilde{\mathcal{N}}^2 \sum_{n,n',m,m'=0}^{\infty} \sqrt{\lambda_n \lambda_{n'} \lambda_m \lambda_{m'}} |n, m\rangle \langle n', m'|_{a_1, b_1} \times \\ &\times \sum_{p=0}^{\min(n,n')} \sqrt{\binom{n}{p} \binom{n'}{p} \epsilon^{n+n'-2p} (1-\epsilon)^{2p}} \times \\ &\times \mathcal{A}_{\sigma}^{(1/2)}(k, n-p) \left( \mathcal{A}_{\sigma}^{(1/2)}(k, n'-p) \right)^* \delta_{\sigma, n+m-p} \delta_{\sigma, n'+m'-p}, \end{aligned} \quad (\text{S39})$$

where we could remove the sum over  $q$ , as only the  $q = 0$  term would contribute to the sum for  $t_a = 1$ .

We may then proceed to act with the Kronecker delta functions. Since  $n + m = n' + m' = S$ , the sum over  $n, m, n', m'$  is in fact bounded by  $S$ . We replace  $p$  with  $S - \sigma$ . As  $p$  must be positive,  $\sigma$  is the lowest value of  $S$ . Thus, the density matrix takes the following form

$$\begin{aligned} \tilde{\rho}_{\text{out}}^{(k,\sigma)} &= \tilde{\mathcal{N}}^2 \sum_{S=\sigma}^{\infty} \sum_{n,n'=0}^S \sqrt{\lambda_n \lambda_{n'} \lambda_{S-n} \lambda_{S-n'}} |n, S-n\rangle \langle n', S-n'|_{a_1, b_1} \times \\ &\times \sum_{p=0}^{\min(n,n')} \sqrt{\binom{n}{p} \binom{n'}{p} \epsilon^{n+n'+2\sigma-2S} (1-\epsilon)^{2(S-\sigma)}} \times \\ &\times \mathcal{A}_{\sigma}^{(1/2)}(k, n-p) \left( \mathcal{A}_{\sigma}^{(1/2)}(k, n'-p) \right)^*. \end{aligned} \quad (\text{S40})$$

Finally, we notice that  $\lambda_n \lambda_{S-n} = \frac{\lambda_S}{\cosh^2 g}$

$$\begin{aligned} \tilde{\rho}_{\text{out}}^{(k,\sigma)} &= \tilde{\mathcal{N}}^2 \sum_{S=\sigma}^{\infty} \lambda_S \left( \frac{1-\epsilon}{\epsilon} \right)^S \sum_{n,n'=0}^S \epsilon^{\frac{n+n'}{2}} |n, S-n\rangle \langle n', S-n'|_{a_1, b_1} \times \\ &\times \sum_{p=0}^{\min(n,n')} \sqrt{\binom{n}{p} \binom{n'}{p}} \mathcal{A}_{\sigma}^{(1/2)}(k, n-p) \left( \mathcal{A}_{\sigma}^{(1/2)}(k, n'-p) \right)^*, \end{aligned} \quad (\text{S41})$$

where the normalization factor equals

$$\frac{1}{\tilde{\mathcal{N}}^2} = \sum_{S=\sigma}^{\infty} \lambda_S \left( \frac{1-\epsilon}{\epsilon} \right)^S \sum_{n=0}^S \epsilon^n \sum_{p=0}^n \binom{n}{p} \left| \mathcal{A}_{\sigma}^{(1/2)}(k, n-p) \right|^2. \quad (\text{S42})$$

We notice that, unlike in Eq. (S31), it is impossible to decompose the matrix into  $\epsilon$ -independent components

$$\tilde{\rho}_{\text{out}}^{(k,\sigma)} = \tilde{\mathcal{N}}^2 \sum_{S=\sigma}^{\infty} \chi_{\sigma,S}(\epsilon) \tilde{\rho}^{(\sigma,k,S)}(\epsilon), \quad (\text{S43})$$

where  $\chi_{\sigma,S}(\epsilon) = \frac{\lambda_S}{\tilde{\mathcal{N}}(\epsilon)^2} \left(\frac{1-\epsilon}{\epsilon}\right)^S$  and the density matrix components are

$$\begin{aligned} \tilde{\rho}^{(\sigma,k,S)}(\epsilon) = & \tilde{\mathcal{N}}(\epsilon)^2 \sum_{n,n'=0}^S \epsilon^{\frac{n+n'}{2}} |n, S-n\rangle \langle n', S-n'|_{a_1, b_1} \times \\ & \times \sum_{p=0}^{\min(n,n')} \sqrt{\binom{n}{p} \binom{n'}{p}} \mathcal{A}_{\sigma}^{(1/2)}(k, n-p) \left(\mathcal{A}_{\sigma}^{(1/2)}(k, n'-p)\right)^*, \end{aligned} \quad (\text{S44})$$

with

$$\frac{1}{\tilde{\mathcal{N}}(\epsilon)^2} = \sum_{n=0}^S \epsilon^n \sum_{p=0}^n \binom{n}{p} \left| \mathcal{A}_{\sigma}^{(1/2)}(k, n-p) \right|^2. \quad (\text{S45})$$

The term  $\epsilon^{\frac{n+n'}{2}}$  acts with the same strength on density matrix entries with constant  $n+n'$ , which corresponds to entries lying on the antidiagonals of that matrix. Moreover, the larger  $n+n'$  for a given antidiagonal is, the more suppressed its elements will be. In addition, as  $\epsilon$  decreases and larger losses are allowed in the system, elements of the matrix corresponding to large photon number events die down in favor of small photon number events, particularly the vacuum and single photon events. The effect is, as if the dimension of the Hilbert space, in which the output states live, was being reduced.

## B. Numerical computations

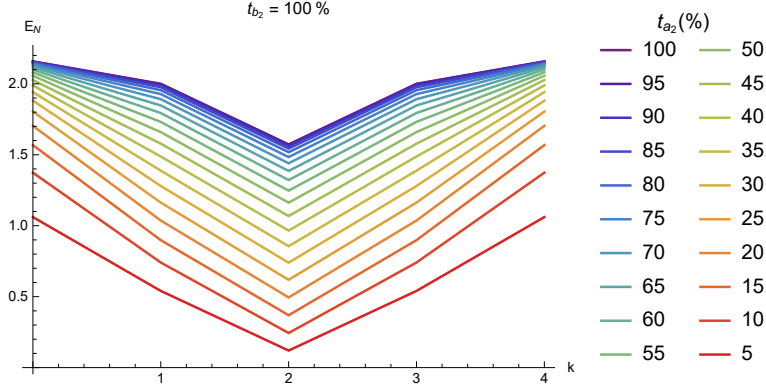


FIG. S11. Logarithmic negativity computed for the state in Eq. S41.

To back up our analytic derivations shown in Section IIIA, we have computed logarithmic negativity for the state given in Eq. S41 for various values of transmittances  $t_a = \epsilon \cdot 100\%$ , while keeping Bob's mode ideal ( $t_b = 100\%$ ). As before, we display transmittances in percentages (%) in the following results.

A representative figure showing the behavior of logarithmic negativity as the transmittance of idler modes is made progressively more unequal is shown in Fig. S11. For the first 3-4 lines from the top, the amount of entanglement decreases only slightly. A significant decrease of quantum correlation can be observed for  $t_{a_2} < 50\%$ .

Further analysis reveals that the entanglement is best preserved for the case where all photons emerge from the same output of the beam splitter, i.e. for  $k = 0, S$ . The entanglement deteriorates quickest when the outputs of the beam splitter are equally populated,  $k = S/2$ . These results are shown in Fig. S12 where the dependence of the logarithmic negativity on scaling of losses  $\epsilon = \frac{t_a}{t_b}$  was plotted. From these calculations it can be inferred that the protocol maintains its quality of output (up to 90% of the maximal value of entanglement) down to  $\epsilon = 0.7$  for  $k = 2$  and  $\epsilon = 0.4$  for  $k = 0$ , assuming  $2S = 8$  photons emerged from the crystals. Moreover, the values seem to follow a logarithmic curve (solid lines in Fig. S12)), which confirms our inference of Hilbert space dimension reduction (we recall that logarithmic negativity for the maximally entangled states is  $\log_2(2\sqrt{S+1} + 1)$ ).

The logarithmic functions were fitted with the following parameters

- $k = 0$ :  $\log_2(-237 + 242 \epsilon^{0.00357})$
- $k = 1$ :  $\log_2(0.901 + 3.37 \epsilon^{0.632})$
- $k = 2$ :  $\log_2(0.842 + 2.37 \epsilon^{0.831})$

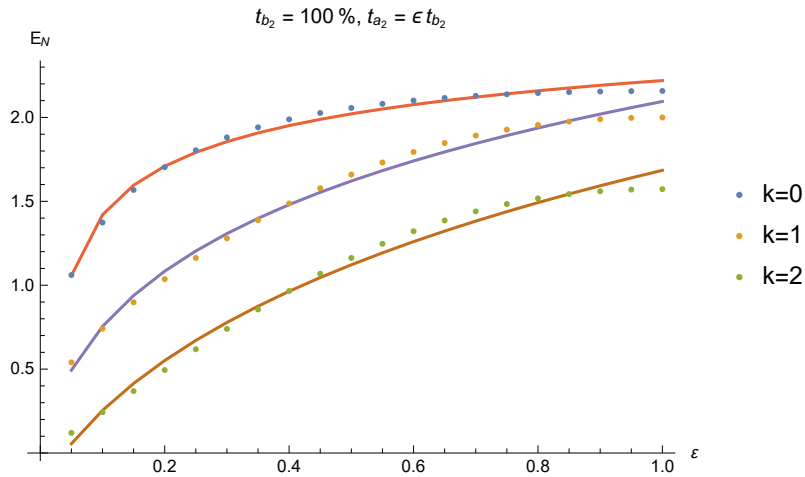


FIG. S12. Dependence of logarithmic negativity shown in Fig. S11 on imbalance of losses in the two idler modes,  $\epsilon = \frac{t_a}{t_b}$ , for  $g = 0.1$  and  $S = 4$ .

### C. Numerical computations with both idler modes lossy

We include computations for the more general cases, when Bob's mode is no longer assumed lossless. The results are shown in Fig. S13.  $t_{b_2}$  takes values from 90% to 10% and for each  $t_{b_2}$ ,  $t_{a_2}$  goes from 5% to  $t_{b_2}$  in steps of 5%. When the transmittances of the two idler modes are equal, the amount of entanglement is close to maximal, given by  $\log_2(2\sqrt{5} + 1) \approx 2.45$ . As the symmetry between the modes is broken, entanglement decreases.

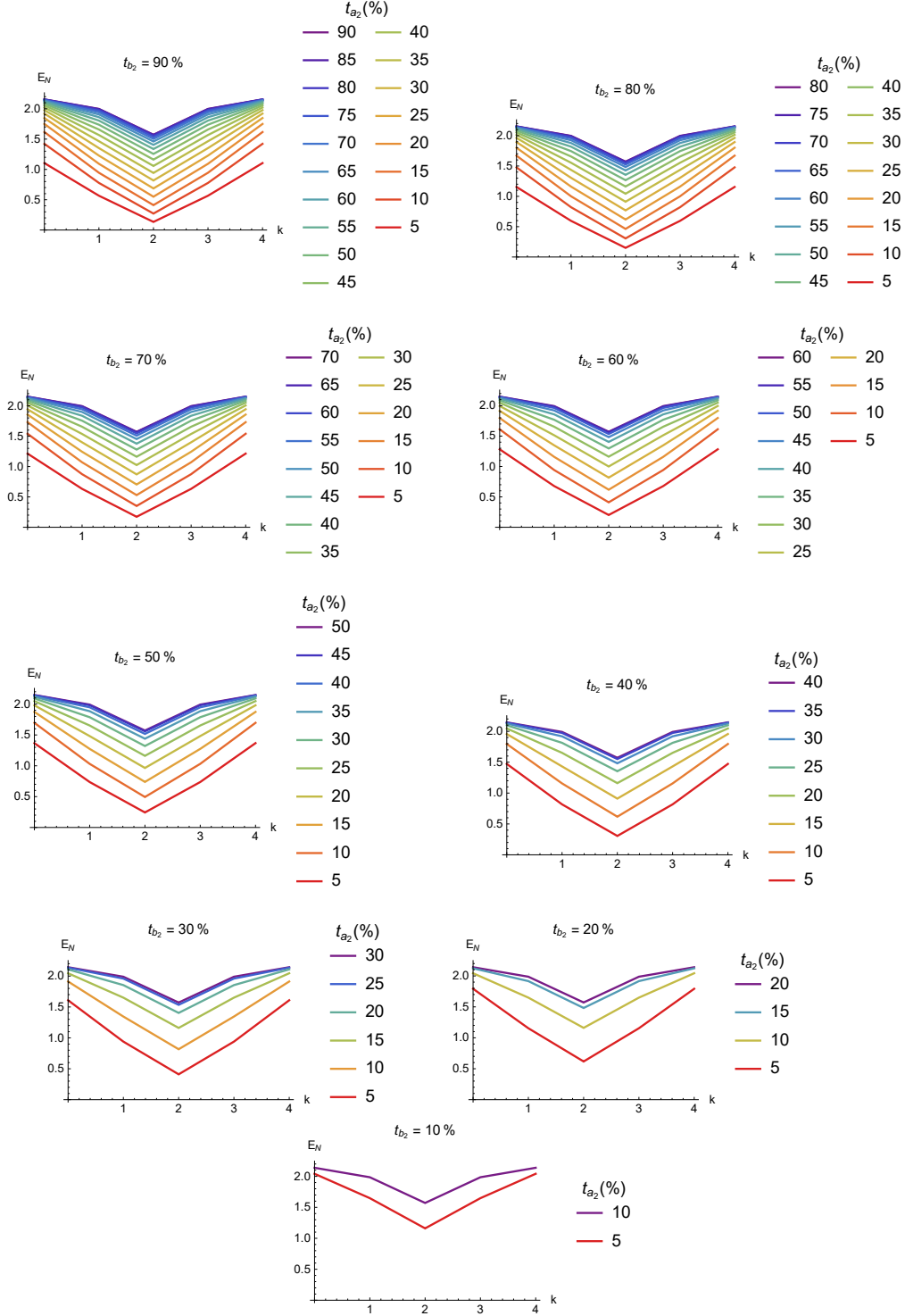


FIG. S13. Logarithmic negativity computed for different pairs of transmittances between idler modes for  $g = 0.1$  and  $S = 4$ .

#### D. General case which assumes losses in all modes and in detection

Finally, we include computations for losses present in all modes and detectors. To this end, we have set different values of  $r_i$  between 0 and 99.999999% while changing losses in signal modes  $a_1$  and  $b_1$  between 0 and 50% as well as keeping losses at the TESs to be 5% or 28%. The results for two representative cases are depicted in Fig. S14. In the case of losses in mode  $a_2$  set to 10% and losses in mode  $b_2$  set to 90% the results are still similar to those presented in Fig. S10. However, setting them to 99.99999% (60 dB) and 99.999999% (80 dB) significantly deteriorates the result, even when losses in signal modes are set to zero.

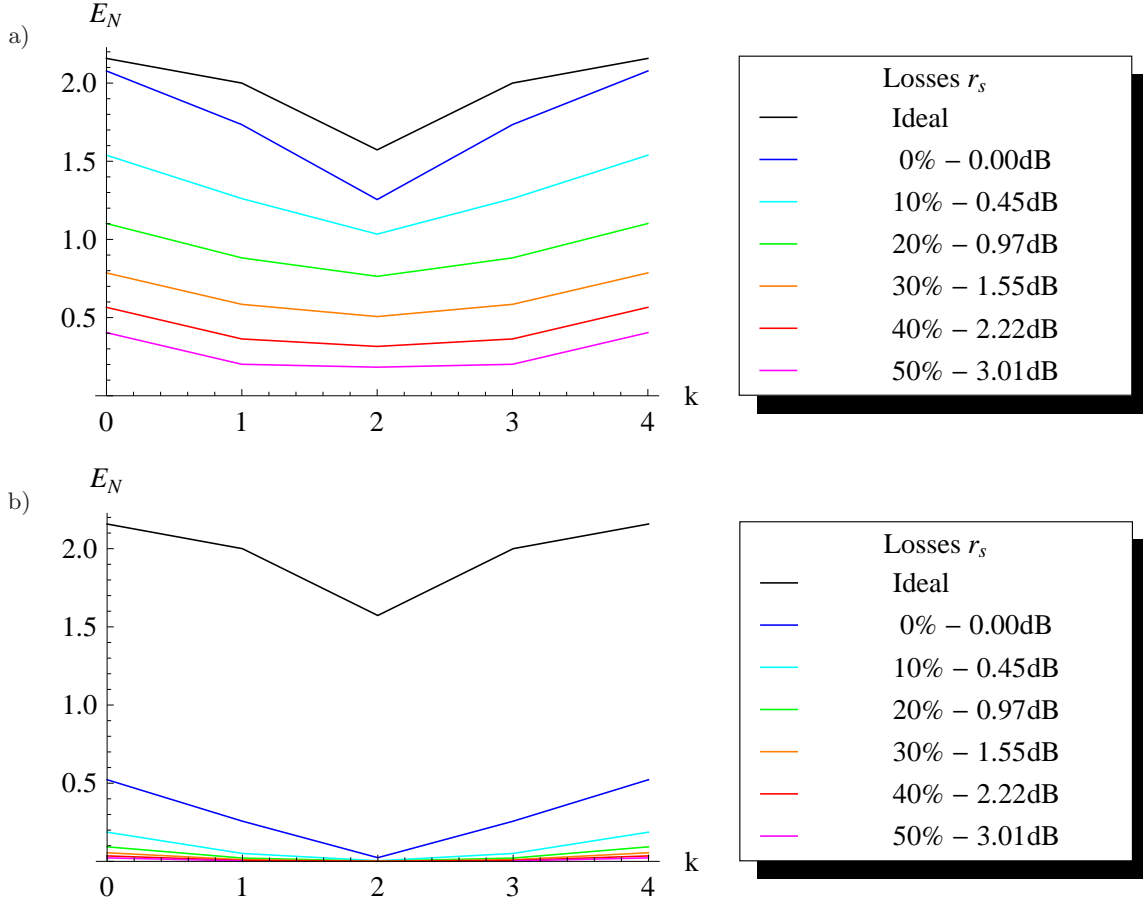


FIG. S14. Logarithmic negativity computed for  $g = 0.1$  and  $S = 4$  assuming unsymmetric losses in modes  $a_2$  and  $b_2$ : a) 10% and 90% b) 99.99999% (60 dB attenuation) and 99.999999% (80 dB). The losses  $r_s$  in signal modes  $a_1$  and  $b_1$  vary between 0 and 50% while losses at the detectors are set to 28%.

#### IV. LOSSES VARYING WITH TIME

As has been discussed in Ref. [25], losses in each mode will vary over time on the timescale of 10-100 ms for losses coming from atmospheric turbulence and 0.1-1 s for losses deriving from jitter in the telescopes. A single pulse traveling towards a satellite on a low-Earth orbit will take approximately 3 ms to reach the satellite. Therefore any fluctuation variations will only affect the time-averaged logarithmic negativity Alice and Bob compute for all successful events.

Let us assume that Bob's modes's transmittance is fixed and the Alices's has a normal distribution with variance 1 dB. We then generate 500 random values from that distribution and calculate the resulting logarithmic negativity. We repeat the process for different values of transmittance  $t_{b_2}$ . An example figure is shown in Fig. S15 for typical attenuation of 80 dB.

We find that the averaged value of logarithmic negativity is only 0.01-0.05 below the maximal value. This is also shown for a wide range of transmittances in Fig S16. The error bars show the maximal and minimal values of the

logarithmic negativity which occurred. We observe that the dependence of the logarithmic negativity on fluctuations is uniform across a wide range of transmittances.

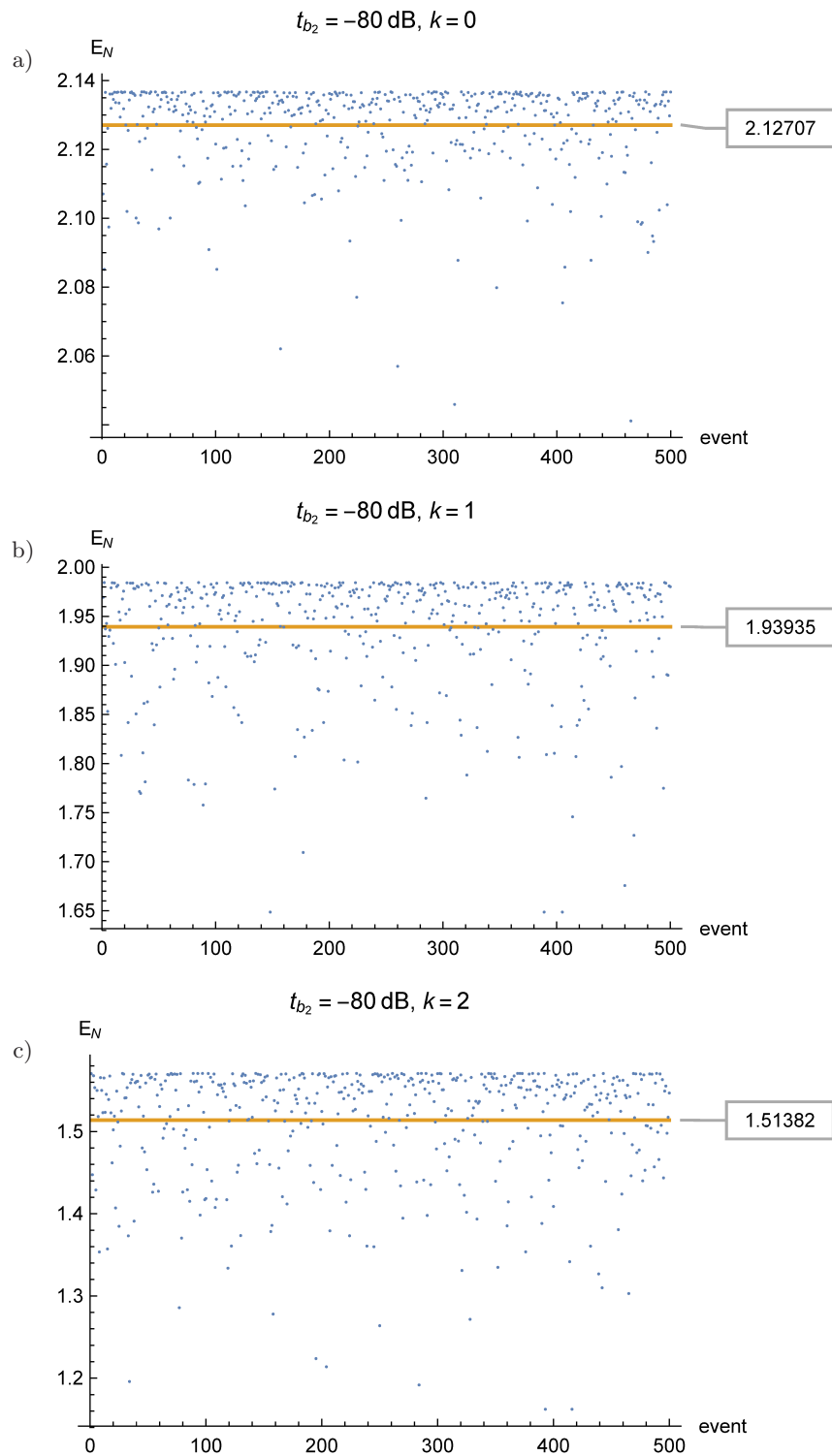


FIG. S15. Randomly generated values of logarithmic negativity for 500 events calculated for 80 dB attenuation and variance 1 dB: a)  $k = 0$ , b)  $k = 1$ , and c)  $k = 2$ .

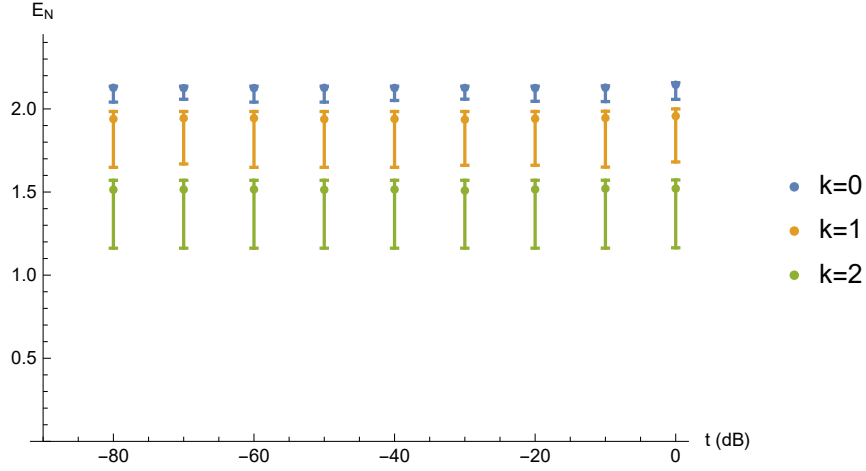


FIG. S16. Dependence of the logarithmic negativity averaged over 500 events assuming fluctuations of 1 dB.

## V. EFFICIENCIES AND SUCCESS RATES

### A. Protocol efficiency in the ideal case

Interference of modes  $a_2$  and  $b_2$  on a BS alters the input state  $|\Psi_{\text{in}}\rangle = |\Psi\rangle^{\otimes 2}$  (described in the main text) in the following way

$$|\Psi_{\text{out}}\rangle = \sum_{n,m=0}^{\infty} \sqrt{\lambda_n \lambda_m} |n, m\rangle_{a_1, b_1} U_{\text{BS}} |n, m\rangle_{a_2, b_2}, \quad (\text{S46})$$

$$\rho_{\text{out}} = |\Psi_{\text{out}}\rangle \langle \Psi_{\text{out}}| = \sum_{n,m,p,q=0}^{\infty} \sqrt{\lambda_n \lambda_m \lambda_p \lambda_q} |n, m\rangle \langle p, q|_{a_1, b_1} \otimes U_{\text{BS}} |n, m\rangle \langle p, q|_{a_2, b_2} U_{\text{BS}}^\dagger. \quad (\text{S47})$$

After tracing out modes  $a_1$  and  $b_1$  we obtain

$$\rho_{a_2, b_2} = \text{Tr}_{a_1, b_1} \{\rho_{\text{out}}\} = \sum_{n,m=0}^{\infty} \lambda_n \lambda_m U_{\text{BS}} |n, m\rangle \langle n, m|_{a_2, b_2} U_{\text{BS}}^\dagger. \quad (\text{S48})$$

Thus, the probability of detecting  $|k, S-k\rangle$  behind the BS equals

$$p_S(k) = \text{Tr} \{|k, S-k\rangle \langle k, S-k| \rho_{a_2, b_2}\} \quad (\text{S49})$$

$$= \sum_{n,m=0}^{\infty} \lambda_n \lambda_m \langle k, S-k | U_{\text{BS}} |n, m\rangle \langle n, m|_{a_2, b_2} U_{\text{BS}}^\dagger |k, S-k\rangle. \quad (\text{S50})$$

Since the beam splitter interaction is particle number conserving,  $S = n + m$  must hold true. In addition, we note that  $\lambda_a \lambda_b = \frac{\lambda_{a+b}}{\cosh^2 g}$  and therefore,

$$p_S(k) = \sum_{n=0}^{\infty} \lambda_n \lambda_{S-n} |\mathcal{A}_S(k, n)|^2 = \frac{\lambda_S}{\cosh^2 g} \sum_{n=0}^{\infty} |\mathcal{A}_S(k, n)|^2 = \frac{\lambda_S}{\cosh^2 g}. \quad (\text{S51})$$

The protocol efficiency depends solely on the parametric gain  $g$  and  $S$ . Fig. S17 shows  $p_S$  for  $g = 0.1$ .

The success rate of obtaining a particular total photon number  $S$  is then calculated from multiplying the protocol efficiency and the repetition rate of the pump. For example, assuming  $g = 0.1$  and  $f_{\text{rep}} = 80$  MHz, we would observe events having  $S = 4$  photons in total with frequency 0.76 Hz and events having  $S = 2$  with frequency 7.7 kHz.

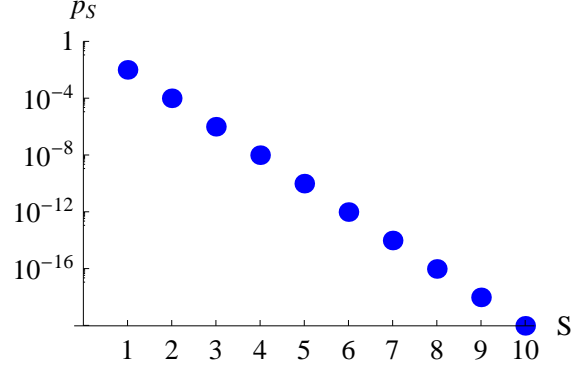


FIG. S17. Protocol efficiency given in Eq. S51 as a function of  $S$  computed for  $g = 0.1$ .

### B. Realistic success rate

The success rate in our protocol is proportional to the probability of receiving at least one photon on the satellite, as then we are certain that Alice and Bob share entangled states. The complement of that event is that no photons reach the satellite, equivalent to  $\sigma = 0$  at the detectors.

Starting from Eq. S24, we take the trace over modes  $a_1$  and  $b_1$ , which sets  $n = n'$  and  $m = m'$ . Then we project the state onto  $|0, 0\rangle_{a_2, b_2}$ . This operation sets  $n = p$  and  $m = q$  and as a result the sums over  $p$  and  $q$  disappear. The probability of nothing reaching the satellite is therefore

$$p_{\sigma=0} = \text{Tr}_{a_1, b_1} \{ \rho_{\text{in}} |0, 0\rangle \langle 0, 0|_{a_2, b_2} \} \quad (\text{S52})$$

$$= \sum_{n, m=0}^{\infty} \lambda_n \lambda_m r_a^n r_b^m \quad (\text{S53})$$

$$= \sum_{n=0}^{\infty} \lambda_n r_a^n \sum_{m=0}^{\infty} \lambda_m r_b^m \quad (\text{S54})$$

$$= \frac{1}{\cosh^4 g} \cdot \frac{1}{1 - r_a \tanh^2 g} \cdot \frac{1}{1 - r_b \tanh^2 g}. \quad (\text{S55})$$

In the case of symmetric losses,  $r_a = r_b = r$ , we have

$$p_{\sigma=0} = \left( \sum_{n=0}^{\infty} \lambda_n r^n \right)^2 \quad (\text{S56})$$

$$= \frac{1}{\cosh^4 g} \cdot \frac{1}{(1 - r \tanh^2 g)^2}. \quad (\text{S57})$$

For a typical parametric gain ( $g = 0.1$ ) and atmospheric losses ( $r = 80$  dB) we obtain  $p_{\sigma \neq 0} = 1 - p_{\sigma=0} = 2 \cdot 10^{-10}$ . Assuming pulse repetition rate of 80 MHz, our success rate will be 1.6 Hz, i.e. 1.6 successful events per second.

## VI. SOFTWARE

The software that we have developed and used was written in Python 3 using the NumPy package, which was employed for matrix algebra. The program performs operations described by the following algorithm

1. for both SPDC sources belonging to Alice and Bob, compute  $\rho_{\Psi} = |\Psi\rangle \langle \Psi|$  where,  $|\Psi\rangle = \sum_{n=0}^{n_{\text{max}}} \sqrt{\lambda_n} |n, n\rangle$ , and  $n_{\text{max}}$  is a sum cutoff found by solving  $\lambda_{n_{\text{max}}}/\lambda_0 < 10^{-15}$  for a given  $g$  and  $10^{-15}$  results from the precision of the numeric data type; usually  $n_{\text{max}} \geq 6$ .
2. for all modes leaving the sources, add losses and then trace out unwanted modes, i.e. perform the following operation

$$\rho_{\Psi'} = \text{Tr}_{3,4} \left\{ U_{\text{BS}}^{(r_s)} U_{\text{BS}}^{(r_i)} |\Psi\rangle \langle \Psi| \left( U_{\text{BS}}^{(r_i)} \right)^\dagger \left( U_{\text{BS}}^{(r_s)} \right)^\dagger \right\},$$



where  $r_s$  and  $r_i$  are losses in signal and idler modes, respectively,

3. construct the density operator matrix for  $\rho_{\text{in}} = \rho_{\Psi'} \otimes \rho_{\Psi'}$ ,
4. apply the 50 : 50 BS operation,  $\rho_{\text{BS}} = U_{\text{BS}} \rho_{\text{in}} (U_{\text{BS}})^\dagger$ ,
5. add losses  $r_{d_1}$  and  $r_{d_2}$  to the modes leaving the BS

$$\rho_{\text{out}} = \text{Tr}_{5,6} \left\{ U_{\text{BS}}^{(r_{d_1})} U_{\text{BS}}^{(r_{d_2})} \rho_{\text{BS}} \left( U_{\text{BS}}^{(r_{d_2})} \right)^\dagger \left( U_{\text{BS}}^{(r_{d_1})} \right)^\dagger \right\},$$

6. for all  $k = 0, \dots, S$  perform the following operations:

- (a) project  $\rho_{\text{out}}$  onto  $|k, S - k\rangle$ :  $\rho_{\text{out}}^{(k,S)} = \langle k, S - k | \rho_{\text{out}} | k, S - k \rangle$  and renormalize the result,
- (b) compute partial transposition of  $\rho_{\text{out}}^{(k,S)}$ :  $\left( \rho_{\text{out}}^{(k,S)} \right)^\Gamma$ ,
- (c) compute eigenvalues  $\{\alpha_k\}$  of  $\left( \rho_{\text{out}}^{(k,S)} \right)^\Gamma$  using routines built into the NumPy package,
- (d) compute the logarithmic negativity

$$E_{\mathcal{N}} = \log_2 \left( 1 + 2 \sum_k \frac{|\alpha_k| - \alpha_k}{2} \right).$$

The advantage of the above algorithm is relatively fast operation at a cost of huge memory requirements because of the large size of the matrices. In the worst case,  $\rho_{\text{out}}$  contains  $n_{\text{max}}^8$  double-precision values (ca. 13 MB for  $n_{\text{max}} = 6$ , 800 MB for  $n_{\text{max}} = 10$ ) and therefore, computations for  $n_{\text{max}}$  as large as 20 or 50 would be impossible. This has been solved by noticing that the matrix contains mostly zeros and that the sum of the number of photons in all modes cannot be simultaneously higher than  $4n_{\text{max}}$ , which allowed us to apply denser packing. Once the final density operator matrix is computed, subsequent computations (step 6) of the algorithm can be performed for all interesting values of  $S$  and  $k$ .